

DESIGN OF A CHARGED HYPERON BEAM TRANSPORT SYSTEM  
AND CERENKOV DETECTOR FOR THE ENERGY RANGE  
150 - 400 GeV

by

A. Roberts and S. C. Snowdon  
Fermi National Accelerator Laboratory,  
Batavia, Illinois 60510

ABSTRACT

The design of a charged hyperon beam to cover the momentum range 150 - 400 GeV/c at Fermilab is investigated. The following conclusions are reached:

1) An achromatic beam design is superior to a conventional dispersive beam; it allows the production of a parallel beam, the use of Cerenkov detectors of much simpler and more powerful design, and particle identification and tagging to higher momenta. In addition, with a conventional detector, a wider momentum range can be accepted.

2) Beams to cover the range 150 - 400 GeV can be designed; the change required to cover this range may be merely retuning, but this is wasteful of decay length. The recommended arrangement is to change the cone angle of the focusing Cerenkov detector from 7 to 11.5 mrad to cover the range, with a corresponding change in length, 15 m and 7 m. Separation of sigma from xi should be feasible to energies of 320 GeV or more.

For the Cerenkov detector, the DISC is rejected as less flexible than the focusing counter. In later phases of the work, if and when CEMA (channel electron multiplier array) image intensifier tubes with segmented anodes becomes available, the system should become capable of simultaneously processing all the hyperons.

3) The reduction in muon background to be expected with a special beam-dumping, muon-deflecting first bending magnet has been investigated, using the program HALO. The residual background is worst at the lowest values of  $\alpha$ ; but even there the background level still seems well within tolerable limits.

4) All magnets, including the beam dump, may use superconducting coils; the quadrupoles require them to achieve the necessary gradients.

## I. DESIGN OF FERMILAB CHARGED HYPERON BEAM

### A. Requirements

The design study to be described is a continuation of earlier studies for a charged hyperon beam, whose results have been embodied in several reports, as well as proposals for experiments<sup>1-5</sup>. It deals only with the production of a beam of charged, tagged hyperons; the experimental equipment for the study of decays and interactions will be treated elsewhere.

Until early in 1975, the general assumption was that a charged hyperon beam would be built in the meson area, replacing the neutral hyperon beam in M2. The beam design therefore used the same large sweeping-analyzing-beam-dumping magnet. The beam design was, in fact, of minimum sophistication; aimed at a maximum momentum of 150 GeV/c, it included only a bending magnet and a quadrupole pair, to give point-to-parallel focusing, but with the momentum dispersion imposed by the bending magnet.

The requirement of a parallel beam is due to the need to identify beam particles. The negative beam contains at least eight different kinds of particles, the positive six, not counting in either case the anti-hyperons present; adding them brings the count to 9 in both cases. Particle identification in such a beam is best done by a focusing Cerenkov detector, which demands a parallel beam. The Yale-NAL-BNL hyperon beam at BNL did not include a Cerenkov detector, (and we sometimes wished it had); the corresponding CERN PS beam did have one. At Fermilab energies, where the additional length required for a Cerenkov detector is far less costly in hyperon decay than at BNL, such a detector is clearly worthwhile.

The design criteria for an ideal charged hyperon beam thus include the following points:

1) Since baryon yields are maximal in the forward direction, the secondary beam should be taken in the forward direction for best signal-to-noise ratio.

2) At any primary proton energy, the secondary beam should be capable of covering a fairly wide range of  $\alpha$  (ratio of secondary to primary momentum.) The yields of different hyperons are known (from our BNL work<sup>6</sup>) to peak at different values of  $\alpha$ .

3) For maximum flexibility it is wise to design for the full range of primary proton energies likely to be available in the next few years, and for as wide a hyperon momentum range as possible. A suitable range is 150 - 400 GeV.

4) The beam should provide for identifying and tagging the various particles composing it. By tagging, we mean providing a prompt electronic identification signal for use in event logic. The ability to simultaneously identify and tag all the particles in the beam is not required; the particles lighter than protons need not be separated, only rejected. The minimum requirement is to tag at least one kind of hyperon at a time; it is desirable to be able to tag more than one, but not essential.

5) The beam characteristics and shielding must be such as to provide an adequate flux of hyperons for experiments without an excessive background. Two different backgrounds are of concern:

the pion (and other light particle) flux in the charged beam, and the diffuse muon background produced in the same target as the hyperons. The total beam flux is limited not so much by the proton beam current or the beam optics, but by the need to individually count beam particles. The muon flux downstream, in drift chambers and other large area detectors, must be tolerable at the full intensity level of the beam; this requirement imposes a need for a special muon-deflecting magnet at the front end of the beam.

6) Since the beam will contain a momentum bite of several percent, it must also include means for measuring the momentum of individual hyperons to at least 0.5%, in order to give sufficiently precise information for kinematic reconstructions.

## B. Decay Lengths

The overriding consideration in beam design is the short lifetime of all known hyperons. The decay lengths are conveniently stated in units of length per GeV/c, since they are proportional to momentum. For  $\Sigma^-$ , the decay length is 3.71 cm/GeV/c; for  $\Xi^-$ , 3.75; for  $\Omega^-$ ,  $2.3^{+.53}_{-.35}$ ; and for  $\Sigma^+$ , 2.00 cm/GeV/c. At 150 GeV/c the  $\Sigma^-$  decay length is thus 5.67 meters, and at 400 GeV/c it is 14.8 meters. At 400 GeV/c one can think in terms of 40 to 50 meter beams of sigmas. The omega decay length imposes a more stringent constraint, since the yields are much lower and the lifetime more uncertain. The most stringent constraint arises at the lowest momentum at which it is desired to work. It is fortunate that the properties of Cerenkov detectors are such that

it is possible to design a flexible optical system to use small cone angles and greater lengths to give better resolution at high energies, and large cone angles and shorter lengths at low energies where the decay is more rapid.

### C. Tagging

The ability to tag individual hyperons (absent in our BNL experiments) allows many experiments otherwise difficult or impossible. An example is the study of branching ratios among different decay modes, which is necessary, e.g., for a study of the  $\Delta I = 1/2$  selection rule. It is this requirement that makes the use of a Cerenkov detector mandatory, despite the additional decay length introduced. However, it is important that the Cerenkov detector have a high efficiency for detecting beam particles; its acceptance should match, or at least approach the beam phase space, otherwise the study of rare particles like the omega is greatly handicapped.

The original dispersive beam first proposed<sup>4</sup> for the hyperon beam suffered severely from this difficulty; particles of a given momentum were parallel, but the dispersion meant that the direction varied with momentum, and this led to efforts to design special Cerenkov detectors of the image-dissecting type<sup>5</sup>, that could cope with this problem. The need for this complexity has now been removed by the introduction of the achromatic beam, which will allow matching to the acceptance of a conventional Cerenkov detector.

#### D. Multiple Tagging

The tagging requirement introduces another possibility at the other end of the scale. The relative abundance of hyperons observed in the negative beam is expected to be about in the ratio  $10^5$ ,  $10^3$ , 1, for  $\Sigma^-$ ,  $\Xi^-$  and  $\Omega^-$  respectively; in addition there is a large accompanying flux of pions and other junk. We must be able to tag each of these three hyperon components correctly. Multiple tagging is not needed for sigma or cascade detection; it would be most useful in allowing rare omega events to be accumulated while studying the more abundant particles.

Multiple tagging is useful in a negative sense, in that it can be used for anti-coincidence signals to give purer tagging signals. In this sense it is an important feature of Cerenkov counter design.

#### E. Mass Resolution

Aside from multiple tagging, the greatest difficulty arises in the need to distinguish particles whose masses are nearly the same and whose velocity differences are therefore small. The most difficult case is of course the separation of sigma from xi. The mass difference is only 10%, and the velocity differences at high energy eventually vanish; there is always a maximum momentum at which separation is feasible for any particular experimental setup. The angular separation  $\Delta\theta$  at a cone angle  $\theta$  is given by

$$\theta\Delta\theta = (m_{\Xi}^2 - m_{\Sigma}^2)/2E^2 = .156/E^2, \text{ E in GeV/c, } \theta \text{ and } \Delta\theta \text{ in rad.}$$

As we will see, we should be able to separate  $\Sigma^-$  from  $\Xi^-$  up to at least 320 GeV/c.



## II. DESIGN OF THE BEAM TRANSPORT

### A. Procedure

The procedure used to investigate the beam design has been as follows:

1) Use of the beam-optimizing program TRANSPORT to determine the magnet characteristics to achieve desired beam performance. TRANSPORT will optimize on any well defined beam parameter, subject to a large variety of constraints. One can specify the proton target dimensions, the acceptable hyperon solid angle, momentum range, and the focusing requirements; magnet aberrations, slits, misalignments, etc. can be introduced; and both first and second order calculations can be made.

2) A necessary supplement to TRANSPORT is TURTLE, a ray-tracing routine which verifies and amplifies the predictions of TRANSPORT by actually tracing rays through the system. TURTLE assumes lumped beam elements whose properties can be described in the usual multipole expansions. To the extent that the beam conforms to these assumptions, its output is correct to all orders. The histogramming facilities of TURTLE allow the phase space of the beam anywhere in the system to be accurately pictured.

3) In addition to the calculation of the beam phase-space parameters, it is also important to determine the flux of background muons that inevitably accompanies any proton target bombardment. In the case of the relatively short hyperon beam this presents special difficulties, since without corrective action the detectors could readily be swamped by high energy muons

impossible to absorb. For this purpose we have adapted to our use the CERN program HALO, which can trace muons arising from pion or kaon decay through any beam transport system using standard transport magnets for which a map of the magnetic field can be supplied. Unfortunately the repertory of standard magnets is based on standard CERN designs, and does not include all the design types one would like to try. For our purposes, it was found necessary to modify HALO by adding a provision to include muons produced directly in the target by the primary protons. At high transverse momenta, such muons are known to be present to an abundance of  $2 \times 10^{-4}$  as compared with the pions; we have assumed the same ratio for the forward direction as well.\* Thus for high-energy pions which enter the beam dump, and which have available only a short decay path, the relative contribution to the muon halo of the directly produced muons will exceed that of the pion decay for energies above  $90 \text{ d GeV}$ , where  $d$  is the decay path in meters.

In order to carry out the HALO calculations, it is necessary to have a fairly accurate idea of the actual iron configurations of the magnets used. This is especially important for the high

---

\*Note added in proof. New data from Adair et al. (private communication<sup>8</sup>) have just been received, which indicate lower yields in the forward direction by factors of 2 to 5, depending on the muon energy. They arrived too late to incorporate in the present report; their effect will clearly be to lower the predicted muon backgrounds by at least a factor of 2 for muons above  $50 - 75 \text{ GeV/c}$ .

energy muons, whose trajectory differs little from that of the main channel.

HALO also allows the insertion of muon absorbers and deflectors of various sorts, so that muon backgrounds can be minimized.

#### B. Beam Layout

Figure II-1 shows a schematic of the proposed hyperon beam. The beam includes a momentum-selecting dipole, BM1, a quadrupole doublet Q1V and Q2H, a reverse bend BM2, and a focusing Cerenkov detector.

The reverse bend is due to a suggestion by C. M. Ankenbrandt<sup>9</sup>, and significantly modifies the dispersive beam originally proposed<sup>4</sup> for Exp. 97. Without the reverse bend the beam may be characterized as a simple dispersive point-to-parallel focusing system, in which particles in a narrow momentum range are essentially parallel, but the beam is dispersed in direction according to their momentum. The introduction of the reverse bend has the effect of allowing the beam to be achromatized over a significant momentum range - several percent - so that the emergent beam is all effectively parallel within this range. The major advantage of this modification is the great simplification and increase of detection efficiency of the Cerenkov detector that follows. A much simpler, more or less conventional focusing detector can now be used, and the phase space of the beam will match its admittance. To achieve this in the dispersive beam required a rather elaborate image-dissecting system<sup>5</sup>. The achromatic design was apparently considered at one time by the CERN group, but abandoned for reasons not entirely clear to us.

The four magnets required would all have magnetic fields as large as can be conveniently achieved, so that their lengths can be minimized. For the required apertures, it appears that conventional quadrupoles would be about twice as long as superconducting ones. For this and a variety of other reasons, including energy saving, initial cost, and operating cost, it seems desirable to look to superconducting magnet designs, and we have concentrated on these.

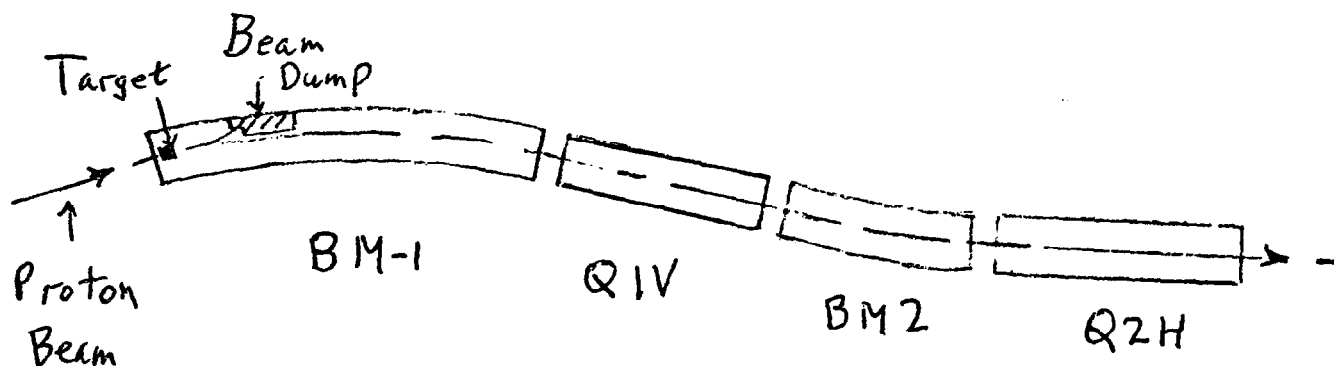


Fig. II-1. Achromatic Hyperon beam, schematic.

The superconducting quadrupole pair require as high a gradient as possible to keep the length down. The final value chosen for the gradient was 10 kgauss/cm (25 kgauss/in) which gives reasonable lengths and promises sufficiently small aberrations.

The first magnet, BM1, combines momentum selection, beam dumping, and muon deflection. It is patterned after a similar magnet<sup>7</sup> used, with much lower intensity proton beams, by experiment E8 in beam M2, for the production of neutral hyperon beams. BM1 is also subject to the constraint that if a superconducting coil is used, the thermal pulse due to radiation from the proton

target must not quench the superconductivity; this appears feasible. The total thermal load due to the beam likewise seems tolerable. The effects of radiation damage on the superconducting coil appear not to be important.

C. Magnet Design: BM1

The length and field strength of BM1 are, in a sense, free parameters for the system; they are not critical. Since the overall shielding and, more important, the muon deflection, depend on them, an overall length of 7.0 m and a 30. kgauss field were decided on when the maximum hyperon momentum contemplated was 240 GeV/c. A few computations were made with a 5 m length; the overall savings in length was only 1.5 m, since longer focusing magnets were required. The longer value seemed desirable both for muon deflection and for shielding. The magnetic field was originally fixed at a conservative 30 kG.

As important as the narrow central field region is the secondary "weak" field region, in which the field is lower but where most of the flux is. This is the part of the magnet, filled with absorber, in which the major portion of the muon halo is deflected away from the downstream detection apparatus. Figure II-2 shows a cross-section of BM1 as presently conceived, and Fig. II-3 a detail of the coil cryostat.

The "weak" field region determines the momentum that muons must have to reach the return yoke before they leave the magnet. Muons that reach it will be deflected back toward the downstream detectors; this momentum limit should be as low as possible.

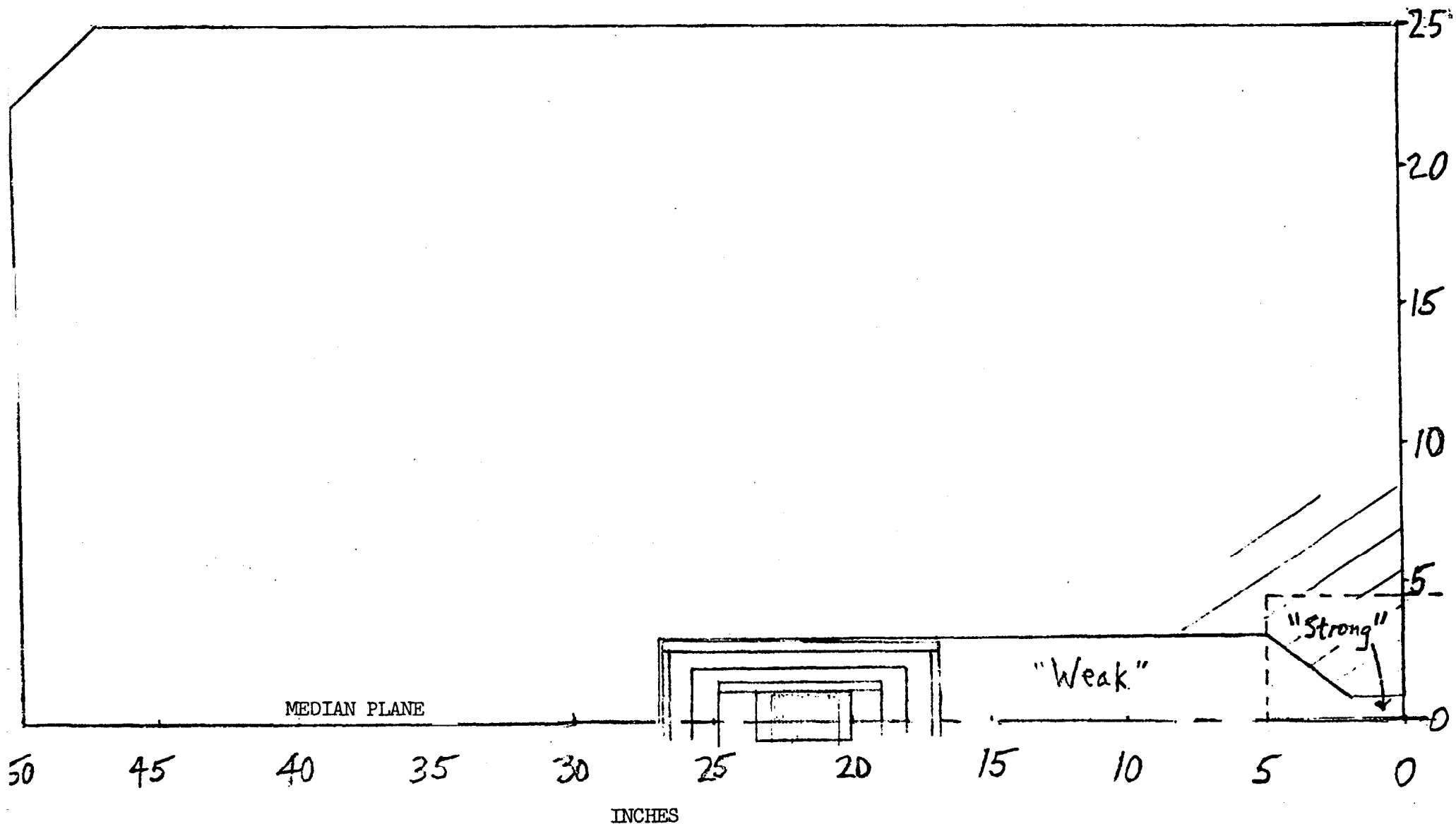


Fig. II-2. Cross-section of BM-1 as presently conceived. One quadrant only is shown. The magnet will separate in the median plane to allow assembly. The central region indicated by dotted lines should be interchangeable to allow target, beam dump, trajectory, and collimation changes. The sagitta of the trajectory is about 1 inch. The "weak" field region, about 19 kG, designed for muon deflection, will be filled with an absorbing material such as zinc. As shown, the magnet would weigh about 170 metric tons.

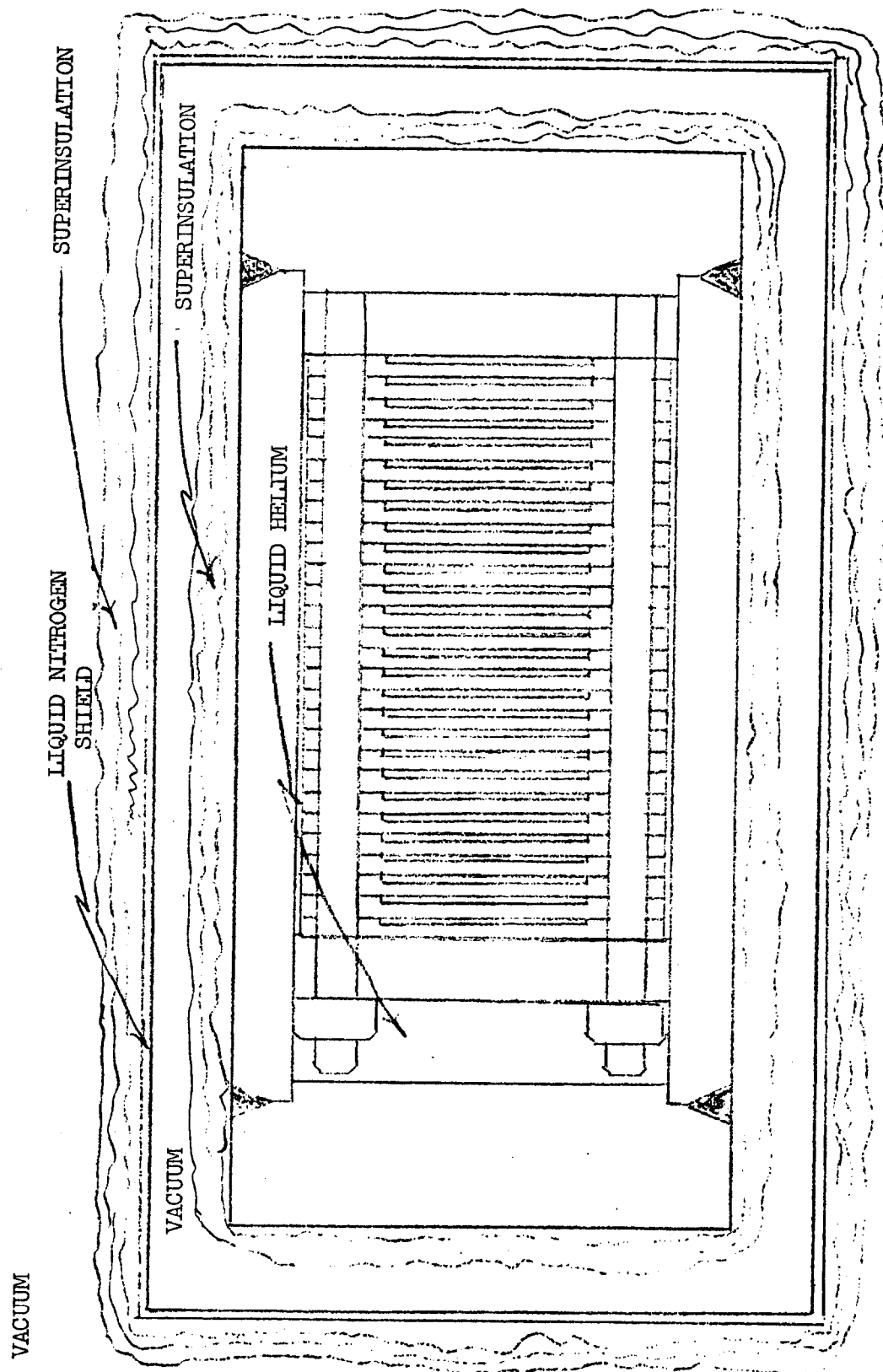


Fig. II-3. Typical Cryostat Cross-Section for Superconducting Dipole BM-1

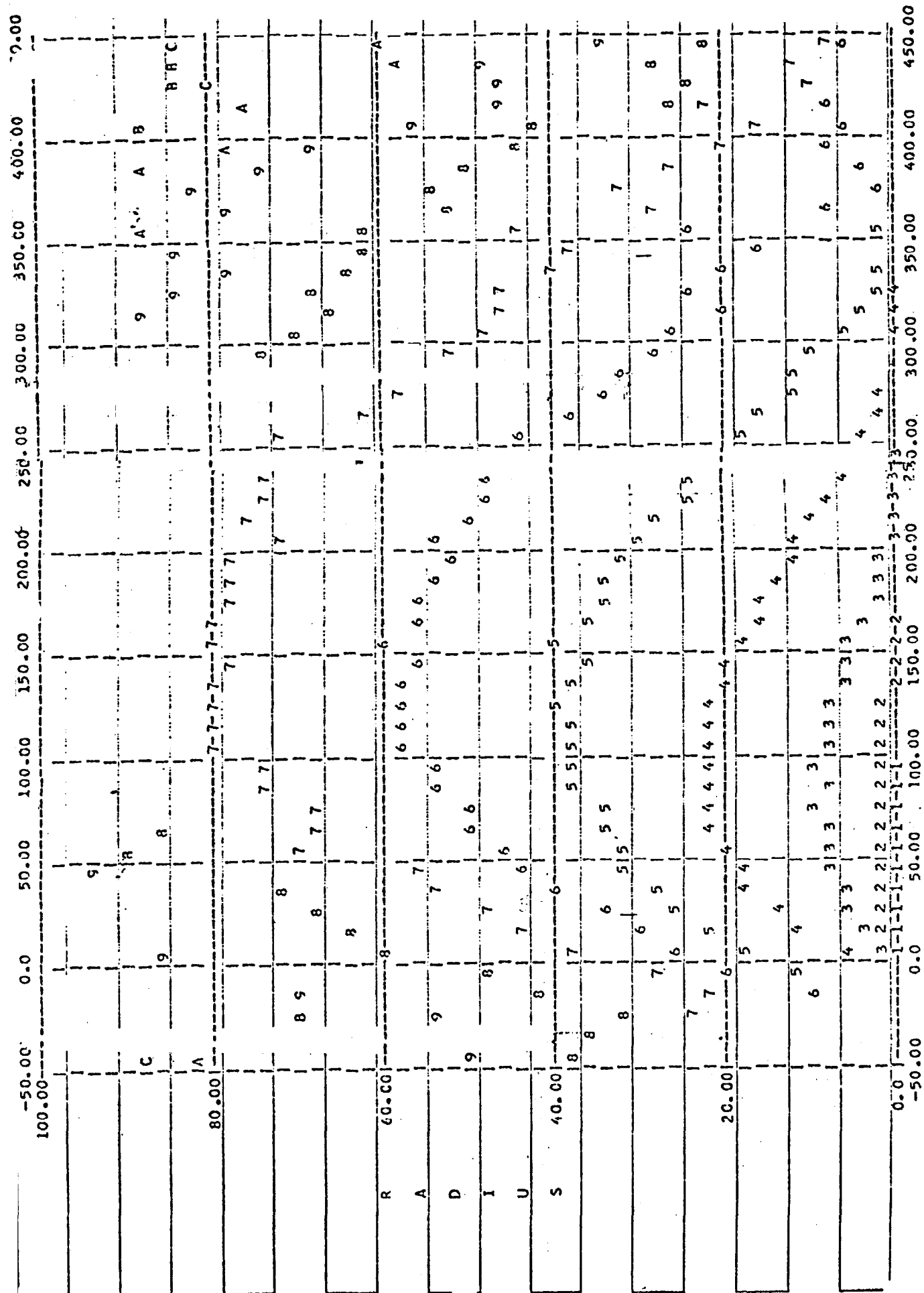
In August 1975 it was decided, in view of probable developments in proton energy to extend the maximum energy of the secondary beam to 400 GeV/c. When this was done it turned out that the 30 kg field and 7 m length gave insufficient dispersion at 400 GeV/c to allow the design of a satisfactory slit system to limit the momentum acceptance. The possible remedies were to increase the length of the magnet or to increase its field. Since by far the greatest fraction of the flux in the magnet is devoted to muon deflection in the "weak" field region (see Fig. II-2) it proved to be possible to increase the field along the hyperon trajectory to 40 kgauss, which is sufficient for our needs.

#### Radiation Quenching

Figure II-4, for which we are indebted to A. Van Ginneken, shows the relative intensity contours for the energy deposited in a large iron beam dump by a 400 GeV/c proton. The contours represent the energy dissipated per unit volume, in  $\text{GeV}/\text{cm}^3$  per incident 400 GeV/c proton. The maximum value at the coil location corresponds to  $10^{-5} \text{ GeV}/\text{cm}^3$ , or  $1.6 \times 10^{-15} \text{ joules}/\text{cm}^3 \cdot 400 \text{ GeV proton}$ . For a  $10^{12}$  proton beam burst, this becomes  $1.6 \cdot 10^{-3} \text{ joules}/\text{cm}^3$  pulse. For copper, density 9., specific heat  $C_p = 1.0 \times 10^{-4} \text{ joules}/\text{gm. degree}$  at  $4^\circ \text{ K}$ , we find  $1.75 \times 10^{-4} \text{ joules}/\text{gm. pulse}$ , giving rise to a temperature rise of just over a degree (the specific heat increases as the cube of the temperature). More important, the pulse is not short enough to be adiabatic provided the magnet is designed with a short thermal time constant. Unpublished experiments by G. Danby<sup>10</sup> on a magnet with a short



CONTOURS OF EQUAL STAR(ENERGY) DENSITY, IN UNITS OF STARS(GEV)/(CM<sup>3</sup>\*INC.PTCLE)  
CONTOUR: ARE SHOWN FOR THE INTEGRAL POWERS OF 10



D E P T H (CM)

R-LABELS REFER TO SMALLER VALUES OF CORRESPONDING BINS

LEGEND: NUMERICAL SYMBOLS REFER TO THE NEGATIVE POWER OF 10 OF THE STAR(ENERGY) DENSITY E.G., 5 REFERS TO THE 10<sup>-5</sup> CONTOUR

Fig. II-4. Energy deposited in a large iron beam dump by a 400 GeV/c proton.

(~ 0.1 sec.) thermal time constant, using beams with a 1 sec. flat top, indicate that a safe limit is about  $6. \times 10^{-4}$  joules/gm. pulse, with quenching at  $3.10^{-3}$  joules/gm. pulse. We conclude that a superconducting coil can be made and used safely. In practice the peak heat load may perhaps be reduced with local tungsten shielding in the weak field gap.

#### Radiation Damage

Superconductors are themselves not particularly susceptible to radiation damage, and the radiation levels in the coils are not thought to offer any hazard to the superconductor or to its associated copper and stainless steel supports. However, one must watch out for insulators, e.g., epoxy. If they cannot be entirely avoided, perhaps they can be kept out of the high intensity radiation regions.

#### Removable Central Region

Like its predecessor, it is envisaged that the central region of BML, comprising perhaps four to eight inches to each side of the center line, and one or two inches of pole face, should be made so as to be removable. This would include a considerable portion of the beam dump, the target, the collimator and slit system. Thus a change of trajectory could be achieved with relative ease; and all critical alignments could be carried out on the bench in a radiation-free environment.

#### Neutral Beams

Since the sagitta of the charged hyperon beam is only an

inch or so, the use of BM1 as a sweeping magnet for a neutral beam appears straightforward. All that is required is to change the central beam section to one with a straight path and corresponding collimation.

D. Quadrupole Pair

The quadrupole pair will have to be superconducting, or else the gradients will have to be drastically reduced, and the quads correspondingly longer. There seems to be no reason why they cannot be superconducting; magnets not too different from the ones proposed have been built at Argonne. At the exit of the bending magnet BM1 we are outside the beam dump, and radiation heating or damage is no longer a serious problem. A design that permits a useful aperture about 3 cm in diameter has been worked out, and is shown in Fig. II-5.

E. BM2

Not too much attention has been given to BM2. It is assumed that the design of a uniform field dipole, with at most a 3-cm gap, and a 40-kG field, with a superconducting coil in a low radiation intensity environment, should not offer any great difficulties. It is desirable, though not essential, for it to be a C-magnet rather than an H-type, if possible; this will tend to decrease the muon flux refocused along the beam.

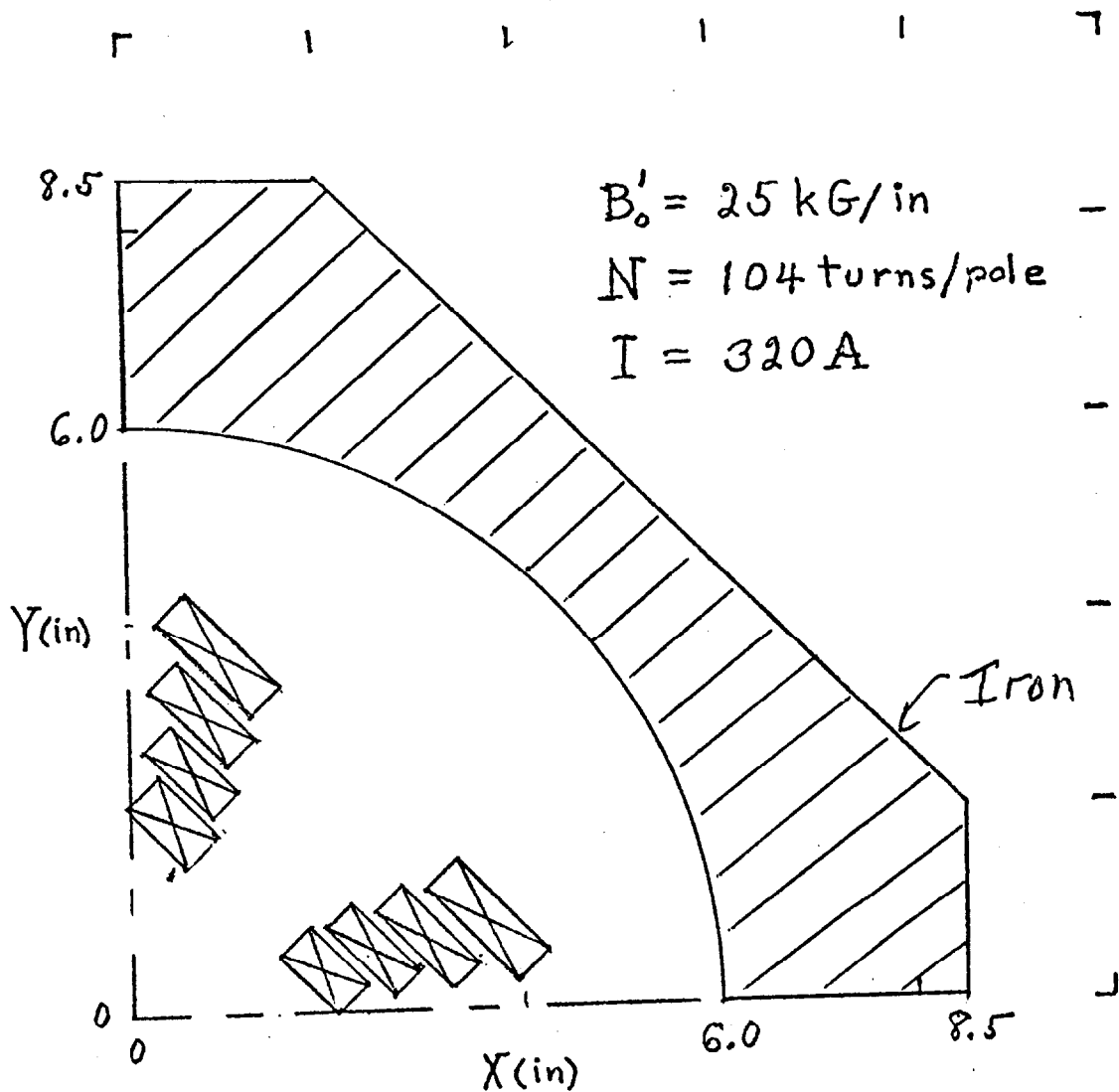


Fig. II-5. Superconducting Quadrupole Cross-Section (first quadrant only)

### III. DETAILS OF BEAM TRANSPORT DESIGN

#### A. TRANSPORT Calculations

A fixed length and field, were postulated for the first bending magnet, BM1. The order of the three remaining components - the quadrupole pair and the reverse bend - was varied, and it was determined that by far the best results came with the vertical focusing quad first, and the horizontal focusing quad last. The criterion for the design was to minimize simultaneously the angular divergence of the outgoing beam and the momentum dispersion. The quantities specified were the dipole fields and the quadrupole gradients and apertures. The quantities varied for optimization were the lengths of the two quadrupoles and the reverse bend. 0.2 m drift spaces separated all magnets.

#### B. TURTLE Calculations

Using the data for lengths thus supplied by TRANSPORT, runs were made with TURTLE to plot the phase space occupied by the beam at various points along it; at first with a "zero phase-space" beam, in which the  $x$ ,  $x'$ ,  $y$ , and  $y'$  ranges of the beam were infinitesimal, and the momentum spread alone allowed to be large; thus the focusing could be examined as a function of momentum. To determine the effects of target size, proton beam phase space, aperture and slit constraints, one then can simply insert these quantities one at a time and observe the effect. Figures III-1 to 6 show a set of such runs for the 400 GeV/c beam. Second-order focusing was used in all runs.

TOTAL NUMBER OF ENTRIES = 10000 INCLUDING UNDERFLOW AND

Fig. III-1. Phase-space plot of  $x'$  vs momentum (in %  $dp/p$ ).

25 cm Target, no slits

TWO DIMENSIONAL PLOT OF XPR VS DP/P

	-4.000	-1.500	1.000	3.500	TOTALS
	I**-----**-----**-----**-----**-----**-----I				
-.150 TO	-.145 I			I	0
-.145 TO	-.140 I			I	0
-.140 TO	-.135 I			I	0
-.135 TO	-.130 I			I	0
-.130 TO	-.125 I			I	0
-.125 TO	-.120 I			I	0
-.120 TO	-.115 I			I	0
-.115 TO	-.110 I			I	0
-.110 TO	-.105 I			I	0
-.105 TO	-.100 I			I	0
-.100 TO	-.095 I			I	0
-.095 TO	-.090 I 11			I	2
-.090 TO	-.085 I 1			I	1
-.085 TO	-.080 I 911			24 I	17
-.080 TO	-.075 I 7822			155 I	30
-.075 TO	-.070 I E9981			14AG I	72
-.070 TO	-.065 I HG9861			122SE I	92
-.065 TO	-.060 I KLC845			449FC I	114
-.060 TO	-.055 I KOFFDA4			1387D<J I	161
-.055 TO	-.050 I FVPFNJ62			59AEMKK I	236
-.050 TO	-.045 I HNUSEIA54			138SAEKUE I	265
-.045 TO	-.040 I OKMRNP1A711			34CCNMWTZ I	350
-.040 TO	-.035 I OPOVOMHH8321			1399CNOVSWQ I	404
-.035 TO	-.030 I PORUSFYOE855			1149FONPPYQIM I	467
-.030 TO	-.025 I SNOKRK\$ZIJJIE2			358EJNQPVXZJQK I	597
-.025 TO	-.020 I KJJJOSPTNVLJ8547C			FDMRS4\$WZUKUHB I	673
-.020 TO	-.015 I CEIHNUU\$YXSXJROMRQ3			UPXWXV1XWSMTG I	878
-.015 TO	-.010 I 63FHMT\$ST\$SS\$Y\$Z\$ST\$ZV\$ST\$SFKE I				1009
-.010 TO	-.005 I 58GLOLQX\$PWX\$33333ZY\$3333\$WRRKJAH I				974
-.005 TO	-.000 I 399ENIPTX\$Z\$333333333333\$USJVEIA94 I				931
-.000 TO	.005 I 346A3JLPUQ\$33333\$W\$33333\$W\$KPRLLBA78 I				879
.005 TO	.010 I 2 87CECFNONY\$33333\$SRX3RLGCA8621 I				705
.010 TO	.015 I 223F9BGMVUSX\$YZ\$33333\$UKNID7945535 I				521
.015 TO	.020 I 32238A89FIKRTNONE0087985312 I				322
.020 TO	.025 I 1 1 3445A78AA6935A43433 3 I				118
.025 TO	.030 I 1 3112 1 I				10
.030 TO	.035 I I				0
.035 TO	.040 I I				0
.040 TO	.045 I I				0
.045 TO	.050 I I				0
	I**-----**-----**-----**-----**-----**-----I				
	I			I	
	I			I	
	I 22232333322333323332233233333232 I				
	I 78909222073133182419802912200927 I				
TOTALS	I 30717668335134639557973055474128 I				9828

TOTAL NUMBER OF ENTRIES = 9828 INCLUDING UNDERFLOW AND

Fig. III-2. Same as Fig. III-1, with 25-cm target, no momentum-defining slits.

25 cm target, with slits

TWO DIMENSIONAL PLOT OF XPR VS DP/P

	-4.000	-1.500	1.000	3.500	TOTALS
	I**-----**-----**-----**-----**-----I				
-.150 TO	-.143 I			I	0
-.143 TO	-.135 I			I	0
-.135 TO	-.128 I			I	0
-.128 TO	-.120 I			I	0
-.120 TO	-.113 I			I	0
-.113 TO	-.105 I			I	0
-.105 TO	-.097 I			I	0
-.097 TO	-.090 I			I	0
-.090 TO	-.082 I			I	0
-.082 TO	-.075 I			I	0
-.075 TO	-.067 I			I	0
-.067 TO	-.060 I			I	0
-.060 TO	-.052 I			I	0
-.052 TO	-.045 I			I	0
-.045 TO	-.037 I			I	0
-.037 TO	-.030 I 1 1			I	2
-.030 TO	-.022 I	1121421 43 11 1 211232 3221		I	41
-.022 TO	-.015 I	57789E696G8AI49973577C769541733		I	239
-.015 TO	-.007 I	3A6C7EJKJILPLOMMNJFJLJGGFA6465		I	461
-.007 TO	.000 I	499EFBJKNOWROUOPSZNUIC90C7F2695		I	510
.000 TO	.008 I	5736FIEL00VMPNKLVLGKCD9998475		I	452
.008 TO	.015 I	124B839JMMJRGXVOKHCF978843		I	366
.015 TO	.023 I	1 34337DAGGEC887354411		I	143
.023 TO	.030 I	4 1		I	5
.030 TO	.038 I			I	0
.038 TO	.045 I			I	0
.045 TO	.053 I			I	0
.053 TO	.060 I			I	0
	I**-----**-----**-----**-----**-----I				
	I			I	
	I			I	
	I	111111111		I	
	I	224356779912121221088666442221		I	
TOTALS	I	29481743861977503980787490166983		I	2219

TOTAL NUMBER OF ENTRIES = 2219 INCLUDING UNDERFLOW AND

Fig. III-3. Same as Fig. III-2, with addition of momentum-defining slits.



TWO DIMENSIONAL PLOT OF YFR VS DP/P

[illegible]

TOTAL NUMBER OF ENTRIES = 10000 INCLUDING UNDERFLOW AND

Fig. III-4. Phase-space plot of  $y'$  vs. momentum (in %  $dp/p$ ).

"Zero" phase-space beam (point target).

25 cm target, no slits

TWO DIMENSIONAL PLOT OF YPR V'S DP/P

	-4.000	-1.500	1.000	3.500	TOTALS
	I**-----**-----**-----**-----**-----I				
-.200 TO	-.190 I			I	0
-.190 TO	-.180 I			I	0
-.180 TO	-.170 I			I	0
-.170 TO	-.160 I			I	0
-.160 TO	-.150 I			I	0
-.150 TO	-.140 I			I	0
-.140 TO	-.130 I			I	0
-.130 TO	-.120 I			I	0
-.120 TO	-.110 I			I	0
-.110 TO	-.100 I			I	0
-.100 TO	-.090 I			I	0
-.090 TO	-.080 I	44 1		1 I	10
-.080 TO	-.070 I	5611		2 135 I	24
-.070 TO	-.060 I	83873421		1 43688 I	75
-.060 TO	-.050 I	006A967331		1243458900 I	142
-.050 TO	-.040 I	CHFDJGEJ353 2		1 58509GIKPG I	281
-.040 TO	-.030 I	MTSHOLKTPFJFAA5 4798MI4F8TORNESR		I	572
-.030 TO	-.020 I	LNQUSIWWOUWVRVSSSS\$UXOVZ\$SJZPL\$J		I	960
-.020 TO	-.010 I	KRUYX\$SSSSZSSSS\$SSSS\$SSSS\$V\$NJ		I	1337
-.010 TO	.000 I	UGUXX\$SSSS\$SSSS\$SSSS\$SSSS\$SSSS\$JTRYO		I	1521
.000 TO	.010 I	LVTXN\$SSSS\$SSSS\$SSSS\$SSSS\$SSSS\$V\$ZSX		I	1546
.010 TO	.020 I	OUSTZ\$SSSS\$SSSS\$SSSS\$SSSS\$SSSS\$Y\$SS\$OYW		I	1310
.020 TO	.030 I	IMUM\$N\$NSUTW\$V\$SS\$N\$SORZJQ\$TSUWQI		I	980
.030 TO	.040 I	LJKRKNRJIHAB\$671346ACIE\$MIOVS\$BH		I	520
.040 TO	.050 I	JKHGGJI879+31		137884HFGHJM I	290
.050 TO	.060 I	H\$FGCA6421		125AA8I9 I	158
.060 TO	.070 I	748A2511		1454499 I	74
.070 TO	.080 I	6352		123 I	22
.080 TO	.090 I	221		1 I	6
.090 TO	.100 I			I	0
.100 TO	.110 I			I	0
.110 TO	.120 I			I	0
.120 TO	.130 I			I	0
.130 TO	.140 I			I	0
.140 TO	.150 I			I	0
.150 TO	.160 I			I	0
.160 TO	.170 I			I	0
.170 TO	.180 I			I	0
.180 TO	.190 I			I	0
.190 TO	.200 I			I	0
	I**-----**-----**-----**-----**-----I				
	I			I	
	I			I	
	I	22232333322333323332233233333232		I	
	I	78909222078133182419802912200927		I	
TOTALS	I	30717658336134639557973055474128		I	9828

TOTAL NUMBER OF ENTRIES = 9828 INCLUDING UNDERFLOW AND

Fig. III-5. Same as Fig. III-4, with 25-cm target, no momentum-defining slits.

25 cm target, with slits

TWO DIMENSIONAL PLOT OF YPR VS DP/P

			-+.000	-1.500	1.000	3.500	TOTALS
			I**	***	***	***	I
-.150 TO	-.140 I						0
-.140 TO	-.130 I						0
-.130 TO	-.120 I						0
-.120 TO	-.110 I						0
-.110 TO	-.100 I						0
-.100 TO	-.090 I						0
-.090 TO	-.080 I						0
-.080 TO	-.070 I						0
-.070 TO	-.060 I	11	1				5
-.060 TO	-.050 I	1	2	421		331 11 1	20
-.050 TO	-.040 I	2	3114223		126243 11		38
-.040 TO	-.030 I	2	43392796345	114422424411223			94
-.030 TO	-.020 I	14342426458FEHH8ECDH9A34554144					242
-.020 TO	-.010 I	12266677E3FJMJNRJTIGD57543363					335
-.010 TO	.000 I	11251778JACMHPURKOKJE7JE A7852463					384
.000 TO	.010 I	436477EGHMJOILL EQNOMFAFA371254					416
.010 TO	.020 I	1322157A9989KNFFPKIFH775978764 2					299
.020 TO	.030 I	134838697AB308F7CG88C6459275 11					231
.030 TO	.040 I	1144244532472321135552554 31231					95
.040 TO	.050 I	122233 4321		2	13331163121		50
.050 TO	.060 I	1 2 11			1 21		9
.060 TO	.070 I	1					1
.070 TO	.080 I						0
.080 TO	.090 I						0
.090 TO	.100 I						0
.100 TO	.110 I						0
.110 TO	.120 I						0
.120 TO	.130 I						0
.130 TO	.140 I						0
.140 TO	.150 I						0
			I**	***	***	***	I
			I				I
			I				I
			I	111111111			I
			I	224356779912121221088556442221			I
TOTALS	I	29481743861977503980787430156983	I				2219

TOTAL NUMBER OF ENTRIES = 2219 INCLUDING UNDERFLOW AND

Fig. III-6. Same as Fig. III-5, with addition of momentum-defining slits.

In addition the effects of magnet aberrations or imperfections could be investigated, as well as end effects and the effects of various beam misalignments.

#### C. RAYTRACE Calculations

Since TURTLE is a matrix procedure using lumped elements, it does not handle end effects and fringing fields explicitly for quadrupoles (it can of course include edge focusing effects for dipoles.) Since the required parallelism of the output beam is rather stringent, it was thought to be worth while to check the results of TURTLE by means of a ray-tracing program, which would automatically be correct to all orders, since it simply integrates the Lorentz equations of motion. The only limit with such a program is that involved in specifying the field accurately enough.

An MIT ray-tracing program, which we renamed RAYTRACE, furnished by S. Kowalski, was used for this purpose. The program is not designed for high energy physics use, but for spectrometers in the 1 GeV region; consequently it is set up with rather different objectives in mind. However, it was found to be usable. The axial rays give results identical to those of TURTLE. The results of other rays, selected to sample the phase space, were in good agreement with TURTLE results. This indicates that the fringing field effects are essentially negligible.

#### D. HALO Calculations

The muon background at the downstream detector position was

investigated by forcing decay of all pions at 0.5 meters from the target. As explained above, it was necessary to add directly produced muons, since they constitute the largest part of the background above 50 to 100 GeV. The design of BM1 is such that all low energy muons are deflected far away from the spectrometer detectors. Only the highest energy muons, which closely parallel the hyperon beam and traverse the hyperon beam transport magnets, contribute to the final background. There is a small flux of very low energy muons (15 GeV and less) that reach the return yoke of BM1 and are deflected back toward the detectors; few in number, they have been ignored). Filling the gap of BM1 with an absorber like Cu or Zn has the beneficial effect of degrading and scattering the muons, thus decreasing the background.

The HALO calculations show that the greatest flux of interfering particles at the downstream detectors is found when the hyperon beam is tuned to energies considerably lower than the incident beam energy, i.e., at low values of  $\alpha$ . In view of these findings, it is not necessary to consider adding special muon deflecting magnets or shields at this time. The major background is that which traverses the iron of the beam transport magnets. It is of relatively high momentum; in fact, near the hyperon momentum.

Figure III-7 indicates the result of a 150 GeV/c HALO run ( $\alpha = 0.5$ ) with all beam magnets in place, with 300 GeV/c protons incident. The plot indicates the geometrical location of halo particles striking a detector plane 52.8 m downstream from the

FLAGS = F5		-500.00	-300.00	-100.00	100.00	300.00	500.00	700.00	SUMS
-300.000 TO	-230.000 I				1	1			I 2
-230.000 TO	-260.000 I								I
-260.000 TO	-240.000 I				1		1		I 2
-240.000 TO	-220.000 I		1		1				I 2
-220.000 TO	-200.000 I			1		1			I 2
-200.000 TO	-180.000 I			1	1				I 2
-180.000 TO	-160.000 I			1	1				I 2
-160.000 TO	-140.000 I		1	2	2	1			I 6
-140.000 TO	-120.000 I		1	1	1	1	1		I 7
-120.000 TO	-100.000 +		11	211	1	1			I 8
-100.000 TO	-80.000 I		1	112	3	1	1		I 10
-80.000 TO	-60.000 I		1	1111	2	1		1	I 11
-60.000 TO	-40.000 I		1	113222112			1		I 18
-40.000 TO	-20.000 I		1	1	11222	1	11		I 15
-20.000 TO	.000 I		2	122	221		1	1	I 15
.000 TO	20.000 I			12322	3	1			I 15
20.000 TO	40.000 I		1	1	232		1		I 11
40.000 TO	60.000 I			1121213	111	1		1	I 17
60.000 TO	80.000 I			112	1	1			I 6
80.000 TO	100.000 +			121	2	1	1		I 3
100.000 TO	120.000 I		1	1	2	1	1	1	I 8
120.000 TO	140.000 I		1	1	11	11			I 6
140.000 TO	160.000 I				1	1	1		I 5
160.000 TO	180.000 I		1	1	21		1		I 6
180.000 TO	200.000 I		2	1	1		1		I 5
200.000 TO	220.000 I		1	1	11	1			I 5
220.000 TO	240.000 I		1		1		1		I 3
240.000 TO	260.000 I			111					I 3
260.000 TO	280.000 I								I
280.000 TO	300.000 +				1				I 1
+-----+-----+-----+-----+-----+-----+-----+-----+-----+ SUMS									S
S									S
U									U
M									M
S									S
11 24053339574474765 1221 2 12 3 13 1311121112									11221 1

Fig. III-7. Muon halo background at a detector plane 52.8 m downstream from the target. Proton beam 300 GeV/c, hyperon beam 150 GeV/c. Horizontal and vertical coordinates in mm. One halo particle represents 1000 muons. The origin is the intersection of the central beam ray with the detector plane.

target. The coordinates are in mm, the origin at the location of the transmitted hyperon beam. Each halo particle represents 1000 muons; the beam is  $3.3 \times 10^{11}$  interacting protons.

We see that the peak intensity, between  $\pm 100$  mm points, reaches 25 halo particles or  $2.5 \times 10^4$  muons in a strip 2 cm wide by 60 cm high at the location of the primary beam. If this is the area covered by a single drift-chamber collecting wire, it indicates that the peak background muon flux averages one particle every 40  $\mu$ sec during the beam spill. A 10 cm lateral displacement will reduce this peak value by a factor of 5. The muon halo spectrum ranges from about 60 to 230 GeV/c, peaking around 110. As noted above, the new data of Adair et al.,<sup>8</sup> indicate that the above numbers are too high by at least a factor of 2.

#### IV. RESULTS OF BEAM DESIGN CALCULATIONS

Three different momenta were used in the principal phase of the design study, and TRANSPORT calculations made for them; most of the preliminary work was done at 240 GeV/c. The major beam parameters obtained are shown in Table IV-1. The quadrupole gradients were 10 kgauss/cm., the bending magnet fields 30 kgauss. Elements are separated by 0.2 m drift spaces.

As may be seen from Table IV-1, the change in field in the dipoles from 400a to 400b does not change the beam optics or magnet lengths. The desired improvement in dispersion is evident only when slits are inserted.



TABLE IV-1

A. Magnet lengths in meters, deflection angles in degrees, for the Achromatic beam, with zero phase space. 400a and 400b refer respectively to runs with the dipoles at 30 and 40 kgauss respectively

Beam Element	Momentum, GeV/c			
	240	320	400a (30 kG)	400b (40 kG)
BM1	7.00	7.00	7.00	7.00
Q1V	1.959	2.540	3.092	3.092
BM2	1.699	1.584	1.486	1.486
Q2H	1.319	1.673	1.996	1.995
Bend, BM1	1.503	1.127	.902	1.203
Bend, BM2	-.365	-.255	-.192	-.256
Total Bend	1.138	.872	.710	.947
Total Beam Length	12.58	13.40	14.17	14.17

B. Parameters for Achromatic Focusing

Momentum, GeV/c	a	b	c
240	0.002	.0012	.0037
320	.002	.0014	.0028
400a	.002	.0006	.0023
400b	.002	.0016	.0032

The parameters for achromatic focusing a, b, and c refer to the empirical equation representing x' focusing:

$$x' = a + by + cy^2 \quad (IV-1)$$

where y represents percent momentum deviation from the central

value, and  $x'$  is in mrad. The momentum values  $y$  at which  $x'$  reaches a given value  $V$  can be obtained by solving the equation

$$y = -b/2c \pm (b^2 + 4vc)^{1/2}/2c \quad (\text{IV-2})$$

E.G., for  $x' = -.018$  at 320 GeV/c, which gives a total span of  $x'$  of .020 mrad, we find the two values of  $y$  are +2.93, - 2.43 (for a zero size target).

It is noteworthy that the rate of change of overall length of the beam with the energy between 240 and 400 GeV/c is almost exactly 1.00 cm per GeV/c. But, as we have seen, the decay lengths of all the hyperons exceed 2. cm/GeV/c. Thus the fraction of hyperons decaying in the beam decreases with increasing energy.

#### A. Contributions to Beam Phase Space from Target Dimensions and Proton Divergence

##### Target Size

The parabola (Eq. IV-1), representing the variation of  $x'$  with momentum, defines the achromatic focusing property of the beam. The other beam properties are simpler; The mean  $x$  coordinate at the output,  $\bar{x}_4$ , changes almost linearly with momentum;  $y$  and  $y'$  do not change. The  $x_4$  dispersion may be characterized as follows:

TABLE IV-2  
Dispersion at End of Beam

Momentum GeV/c	Rate of Change of $x_4$ with Momentum
240	-0.35 cm/% dp/p
320	-0.30 cm/%
400	-0.24 cm/%

These numbers are relevant to the measurement of individual particle momenta in the beam, as we will see later on.

To determine the effect of target size, the point of origin of the beam was displaced from the origin of coordinates in one dimension and the effect on the beam dimension observed. As might be anticipated,  $x$  affects mainly the conjugate coordinate  $x'$ , and similarly  $y$  mainly  $y'$ . The coupling between  $x$  and  $y$  is very small. In like fashion,  $x'$  determines final  $x$  and  $y'$  the final  $y$ . The effect of target height and width can be summarized as follows:

TABLE IV-3  
Variation of Beam Divergence with  
Target Parameters

	E, GeV/c = 240	320	400
a. Variation of $x'$ with horizontal target displacement $x, = x''$	$x'' = .05 \text{ mr/mm}$	.044	.044
b. Variation of $y'$ with vertical target displacement $y, = y''$	$y'' = .20 \text{ mr/mm}$	.20	.20

#### Target Length

Investigation of the effect of target length on focusing properties shows that there is practically no observable effect from moving the source axially 10 cm in either direction from its initial position at the entrance to BML. However, there is another important effect, in that the effective target height and width change with location along the target if the primary proton beam is not perfectly parallel - which of course it is not. This is illustrated in Fig. IV-1.

#### Proton Beam Phase Space

Table IV-4 shows values quoted to us as nominal optimum values to use for the phase space of the incident proton beam in Proton Central<sup>11</sup>. They can be expected to show variations, of perhaps as much as a factor of 2.

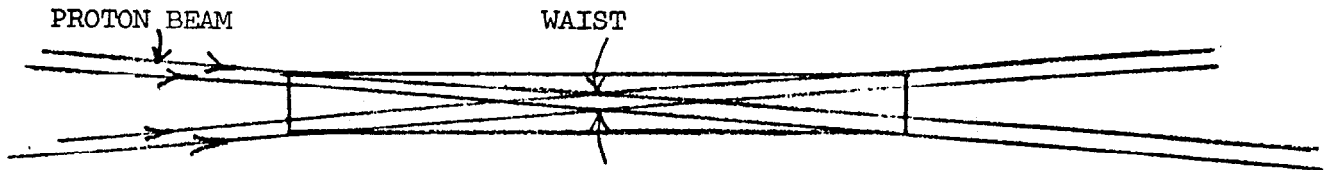


Fig. IV-1. Target illumination by the incident proton beam.

TABLE IV-4

Proton-Central Beam Phase Space

---

Horizontal proton beam admittance:

Phase space area  $0.25\pi$  mm. mrad

Vertical proton beam admittance:

Phase space area  $0.10\pi$  mm. mrad

---

---

It can be shown that the minimum contribution to secondary beam angular width will be obtained when the contributions due individually to minimum beam height and to increase of height in the target (because of primary beam angular divergence) are equal. Thus optimum shape of the primary beam phase space will depend upon the target length as shown in Fig. IV-1. Table IV-5 shows the contribution to angular spread in  $y'$  due to target length  $l$ , and thickness  $t$ , and in  $x'$  due to target width, assuming the contribution suitably minimized.  $y_0$  and  $\theta_y$  are the coordinates of the proton beam vertical phase space,  $x_0$  and  $\theta_x$  of the horizontal.

TABLE IV-5  
Contributions to Angular Divergence  
from Target Length

A. Vertical Divergence:  $y'' = 0.20$  mrad/mm (at all energies)

Length, l	$y_0$	$\theta_y$	t	$y'$
100 mm	0.1 mm	1.0 mr	0.2 mm	0.04 mr
200 mm	.14	.707	.28	.056
250 mm	.157	.64	.314	.063

B. Horizontal Divergence: Take  $x'' = 0.048$  mr/mm as average at all energies

Length, l	$x_0$	$\theta_x$	t	$x'$
100 mm	.158 mm	1.6 mr	.316 mm	.016 mr
200 mm	.224	1.1	.45	.022
250 mm	.25	1.0	.50	.024

These contributions are quite unequal, due to the much greater sensitivity of the beam to vertical height than to horizontal width. There is, however, another source of divergence that contributes to horizontal width alone, thus tending to equalize the divergence. As we have seen, this is the beam momentum spread and the imperfect achromatization.

## Proton Beam Steering

Since the secondary beam is so narrow, it will clearly be necessary to provide steering magnets to allow the proton beam to be accurately directed at the target. Control of both position and direction will be required.

### B. Contributions due to Momentum Width

The momentum width permitted in the beam contributes to the loss of angular resolution in two ways. One is the failure to achieve perfect achromatization described above; the other is a change of radius of the Cerenkov ring, since the cone angle is a direct function of particle velocity. This decreases the separation of particles of different masses.

Table IV-6 summarizes these effects at 240 GeV. At higher energies these quantities are somewhat reduced.

TABLE IV-6  
Effects of Target and Beam Size and Momentum  
Spread at 240 GeV

---

Target Size: 250 mm x 1 mm x .32 mm. Values shown are full widths at about 90% area.

$\Delta x'$ min	.05 m
$\Delta x'$ for $\pm 2\% \delta p$	.065
$\Delta x'$ for $\pm 3\% \delta p$	~ .08
$\Delta y'$ min	.06
$\Delta y'$ for $\pm 2\% \delta p$	.07
$\Delta y'$ for $\pm 3\% \delta p$	~ .08

---

### C. Effects of Magnet Imperfections

#### 1) Dipoles

The effect of sextupole components in the two dipole fields was investigated. In BM2 a sextupole has a much smaller effect than in BM1, as might be expected; an amplitude of .001 (0.1% field error 1 cm from orbit) was unnoticeable. A sextupole field of amplitude .001 in BM1, on the other hand, increased the defocusing of off-momentum particles by a factor between 2 and 2.5; it acts to decrease the achromatization by about 30%. The effect can be seen in Table IV-7, which shows how the focusing is affected. For this table, the value of  $x'$ , the horizontal angular coordinate, is treated as a parabola, as we did above in discussing achromatic focusing. The result of the sextupole aberration is to change the coefficients of the parabola.

TABLE IV-7

Sextupole Effect on Achromatization at  
240 GeV/c

<u>Parameter</u>	a	b	c
No sextupole	.002	.0012	-.0037
Sextupole = .001	.002	.0039	-.0075

An  $x'$  range of .03 mr allows a 5.7%  $\delta p/p$  range with no sextupole; 4.0%  $\delta p/p$ , 30% narrower, with .001 sextupole.

#### 2) Quadrupole Imperfections

Sextupole components in the quadrupole field had similar but much smaller effects. In addition, the effect is sensitive to



the phase of the quadrupole field (rotation) with respect to the sextupole field; it is much smaller when the two are in phase. The major effect was the introduction of a slight variation in the mean  $y'$  with momentum; but this is much smaller than the spread in  $y'$  from other causes.

D. Effect of Misalignments

We have investigated the effect of displacements and rotations on individual magnets, and on the beam as a whole (excluding BM1 which is regarded as fixed.) Displacements and rotations cause angular displacements and tilts, respectively; the effect when the entire transport (two quads and BM2) is simultaneously displaced being a third to a quarter as great as the effect of the single most sensitive component, which depends on the coordinate examined. It is therefore highly desirable that the two quads and the bending magnet, which have an overall length of about 7 meters, be mounted upon a single fixed base, and individually aligned with respect to it; then motions of the base will have much less effect on the particle beam. Displacements of 0.5 mm have noticeable effects on the beam direction; the  $y$  displacement is much more sensitive than  $x$ , as is to be expected from the target sensitivity. It will be necessary to provide means for monitoring and adjusting the beam transport location.

Table IV-8 shows the effect of some misalignments. Small changes in mean direction  $x'$  and  $y'$  are of little consequence; such small displacements provide a method for steering the beam accurately. Large changes introduce chromatic effects which should be avoided.

TABLE IV-8

Effects of Misalignment of Entire Beam

Misalignment	Momentum, GeV		
	240	320	400
x displacement = 1. mm (entire beam)	x' shift = -.05 mrad	x' shift = -.046 mr	x' shift = -.042 mr
y displacement = 1.0 mm	y' shift = -.21 mr	y' shift = -.20 mr	y' shift = -.19 mr
Rotation, 1. degree	y slope = .0025 cm/1% dp/p	y slope = .0025 cm/1% dp/p	y slope = .0025 cm/1% dp/p
	y' slope = .003 mr/1% dp/p	y' slope = .0022 mr/1% dp/p	y' slope = .0018 mr/1% dp/p

#### E. Determination of Individual Particle Momenta

As anticipated in our preliminary report, it has proved to be possible to determine the momenta of individual particles in the beam by correlating their x coordinates at two points in the beam. It turns out the best place to make these observations is at  $x_1$ , just after BM1, and  $x_4$ , at the end of the beam transport, at the entrance to the Cerenkov counter. Accurate location at the latter point is required in any case to obtain the final particle direction. The correlation is capable of yielding reasonably good accuracy in momentum, provided one has detector planes of sufficient accuracy. Table IV-9 shows the precision obtained with a 25 cm. target. The width is due almost entirely to target size; the resolution can readily be improved by reducing the target size.

TABLE IV-9

Momentum Resolution at 240 GeV/c

from  $x_1$ ,  $x_4$

---

All runs made with 25 cm. target:

1.4 mm slit at 3.5 m, 2.8 mm slit at 7. m,  
7. mm slit after BM2.

FWHM in  $x_1$  at a single momentum: 0.014 cm.

$(\Delta x_1 / \delta p/p)_{x_4 = \text{constant}}$  : 0.023 cm/1%  $\delta p/p$

Momentum resolution:  $0.014 / .023 = 0.6\%$   
FWHM

---

#### F. Beam Solid Angle, Acceptance, and Particle Yields

To calculate the flux of secondary particles in a given beam it is necessary to know the production function, and the solid angle. No direct data on charged hyperon production at Fermilab energies is available; the highest energies for which production data are available is 31 GeV, from our BNL run. In addition there are now some data on neutral hyperon production at Fermilab. For the purposes of this report the direct production cross-sections can be taken as those predicted by the Wang formula<sup>13</sup>, with sufficient accuracy. This is most useful not only for the overall yield functions, but for the angular distributions as well. At the energies under consideration the yield falls off so rapidly with angle that it is easy to design beams with angular acceptances large compared to the width of the angular distributions.

Figure IV-1 (p. 37 ) shows the target illumination produced by the divergent proton beam. The horizontal spread of the proton beam is large ( $\pm 1$ . mrad) compared to the secondary beam acceptance (less than 0.5 mrad) so that the secondary beam phase space is uniformly filled, though not with equal efficiency, by all incoming protons. However, the proton beam divergence in the vertical plane is only  $\pm 0.64$  mrad for a 250 mm long target, and 1. mrad for a 100 mm target. These numbers are small compared with the acceptance possible in the vertical plane, which is at least  $\pm 2.0$  mrad. Table IV-10 shows the angular distribution function in the Wang production formula, which is a simple exponential function  $\exp (-4.247 p_t)$ , where  $p_t$  is the transverse momentum of the (negative) secondary particle, in GeV/c. From this universal function, the following table can be made.

TABLE IV-10

Angular Production Function from the Wang Formula

$$F = \exp (-4.247 p_t)$$

Particle Momentum, GeV/c	Production Angle, mrad:				
	0.	0.5	1.	1.5	2.0
150	1.00	.727	.529	.385	.280
200	1.00	.654	.428	.286	.183
240	1.00	.601	.361	.216	.130
320	1.00	.507	.257	.124	.066
400	1.00	.428	.183	.078	.033

The total production can be found by integrating the angular function out to infinity, giving the value  $1/4.247 = .236$ . Thus the area is that contained in a uniform distribution out to a transverse momentum of .236 GeV/c. The corresponding production angle is just this quantity divided by the beam momentum. Thus, at 236 GeV/c the total angular distribution is that contained in a 1 mrad angle, or in  $\pi$  microsteradians. In the vertical direction the acceptance may extend well beyond this angle, so that the entire production is contained; in the horizontal direction, the large proton beam divergence ( $\pm 1$ . mrad) and the small equivalent horizontal acceptance, about  $\pm .25$  mrad, cut down the yield. Consequently it seems expedient to change the horizontal proton focusing to get less divergence.

The optimum horizontal focusing was defined as that giving the smallest target size. It was found at a waist of  $\pm .25$  mm and a divergence of  $\pm 1.0$  mrad, giving a horizontal target width of  $\pm .50$  mm. If we depart from the optimum and make the waist  $\pm 0.4$  mm, the divergence  $\pm .625$  mrad, we get a target width of  $\pm .56$  mm, but now the secondary beam angles with the primary proton direction are much reduced, with correspondingly increased yields. There is no sacrifice in resolution either, since the  $x'$  width is smaller than the  $y'$  in any case.

We thus end up with the following table of calculated  $\pi^-$  yields, IV-11. In this table, we have used the Wang formula; we have converted the yields to be per  $\mu\text{sterad} \cdot \text{GeV} \cdot 0.37 \times 10^{12}$  interacting protons, where 0.37 is an assumed target efficiency; this yield we call N. In addition we introduce an angular yield

function  $f_0$ , which depends only on the secondary beam momentum; it is the effective solid angle available to the secondaries ( $= .236/E$ ), multiplied by 0.5 to account for the loss of acceptance in the horizontal direction. The final calculated yield is then  $Y_f$ , the product of these factors.

TABLE IV-11

Overall Yield Calculation for Negative Pions

Secondary Particle Momentum GeV/c	$f_0$ , Corrected Angular Yield	Final Yield: No. of $\pi^-$ /GeV/c. $37 \times 10^{12}$ interacting protons.			
		$E_p = 400$ GeV		$E_p = 500$ GeV	
		$N_p$	$Y_f$	$N_p$	$Y_f$
160	.735	7.0 E07	5.1 E07	11.0 E07	8.0 E07
240	.49	2.7 E07	1.3 E07	7.6 E07	3.7 E07
320	.37	3.7 E06	1.4 E06	2.4 E07	8.7 E06
400	.30	--	---	4.4 E06	1.2 E06

To convert from pions to hyperons we use the following ratios, which for simplicity we assume independent of  $\alpha^*$ ; this does not introduce errors as large as a factor of 2. In addition we need decay factors, which depend upon the beam length and the particle momenta.

\* This is somewhat inaccurate for  $\Sigma$ 's, where yield is lower below  $\alpha = 0.8$ , higher above 0.8. For  $\Xi$  it is quite good (the  $\Xi$  yield being almost identical with  $K^-$ ). For  $\Omega$  there are no data, and the number given is a guess.

TABLE IV-12  
Ratio of Hyperon to Pion Yield  
(assumed independent of  $\alpha$ )

- 
1.  $\Sigma^-/\pi^- = 1.0$
  2.  $\Xi^-/\pi^- = 0.02$
  3.  $\Omega^-/\pi^- = 2. \times 10^{-4}$
- 

We now combine all these factors in Table IV-13 to get final yield figures.

TABLE IV-13  
Hyperon Yields, taking into Account Production and Decay.  
No. of Particles/μster · GeV/c/.37 x 10<sup>12</sup> Interacting Protons.

Proton Mom. GeV	Hyp. Mom.	Total Beam Length	Pion Yield	Decay Factor			Hyperon Yield		
				Sigma	Xi	Omega	Sigma	Xi	Omega
400	160	21.5 m	5.1E7	.0266	.0278	.0029	1.26E6	2.8E4	29.6
400	240	21.5	1.3E7	.0893	.0917	.0203	1.2E6	2.4E4	53.0
400	240	29.5	1.3E7	.0363	.0377	.0048	4.7E5	1.0E4	12.5
400	320	29.5	1.4E6	.0834	.0856	.0182	1.2E5	2400	5.1
500	400	29.5	1.2E6	.137	.137	.0408	1.6E5	3300	9.8

TABLE IV-14

Ratio of Hyperons to Pions at Beam Exit

Beam Momentum GeV/c	Sigmas per $10^6$ pions	Xis per $10^6$ pions	Omegas per $10^6$ pions
160	4.2E4	860	1.2
240 (21.5 m)	8.1E4	1700	3.5
320	8.5E4	1700	3.7
400	1.2E5	2400	6.7

Note: At 400 GeV/c a momentum acceptance of  $\pm 3\%$  would cover a range of 24 GeV/c; the beam would then have to hold to  $4 \times 10^{10}$  incident protons to keep the total particle flux down to  $10^6/\text{sec}$ .

Note on Further Reduction of Muon Background

Since the increase of muon background at low momenta comes from decreasing the field in BM1 and thus failing to deflect the muons adequately, it should be possible to circumvent this difficulty, if necessary, by keeping the field in BM1 at a high value and changing the central plug to give a more curved trajectory. The rest of the beam will have to be retuned, but with more deflection the beam performance should improve. To avoid moving the beam transport, magnets to deflect the incident proton beam could be used to compensate for the change in position of the target.



## V. DESIGN OF THE CERENKOV DETECTOR

The design of the Cerenkov detector takes as its starting point the physics requirements of the experiment. We take it as required to separate and identify hyperons to energies as high as possible - up to 400 GeV/c if possible. To do this implies a focusing type of detector with ring images. Threshold counters in this momentum range are far too long.

### A. Angular Resolution

The angular resolution that determines whether two different ring images are separable is the product of contributions from the beam, and from the Cerenkov detector itself. We have already considered the former; the latter contains several important components.

### Counter Contributions

1) Variation of diameter of ring image with particle momentum. This effect limits the momentum acceptance to a maximum of about  $\pm 3\%$  or less, if sigma-xi separation is to be retained. However, this imposes no great hardship, since in practice we will almost certainly not require so large a momentum bite. However, the slits available for momentum restriction in the beam are not infinitely sharp, and there is always a tail in the momentum pass-band; this is not expected to be troublesome. The sigma-xi separation is always equivalent to a change in momentum of 10%, at any energy or cone angle.

2) Chromatic dispersion in the gas is always the most serious aberration; it enters through the variation of  $n$  in the basic

equation  $\cos \theta = 1/n\beta$ . It is this quantity that dictates the choice of cone angle. By using the least dispersive gases - helium or neon - and limiting the wavelength region used, the chromatic aberration is kept under control.

3) Multiple scattering in the gas, windows, etc. This is negligible in all practical cases, for the momentum ranges under consideration.

4) Optical imperfections and aberrations. These must be kept sufficiently small not to make significant contributions to image width; there are no difficulties in meeting the requirements.

Table V-1 shows the width of a ring image due to chromatic dispersion in He (for which it is minimal) for the wavelength range 280 - 440 nm, for three different cone angles. For comparison we show the angular separations  $\Delta\theta$  of  $\Sigma^-$  and  $E^-$  rings as well. The angular spread of the 240 GeV/c beam was given in Table IV-1; it is .06 - .08 mrad, depending on the momentum bite and target size, and decreases only slightly at higher energies.

We have included for comparison the corresponding data for the DISC counter now available at Fermilab; here, of course, the chromatic aberration has been essentially removed, leaving as the major limitation the restricted angular acceptance.

Figure V-1 shows the separation of sigma from xi graphically, for 7 and 11.5 mrad cone angles.

For these small cone angles, the gas pressure in the counter is always low. At 150 GeV/c, 11.5 mrad, it reaches a maximum of about 3 atmospheres (absolute).

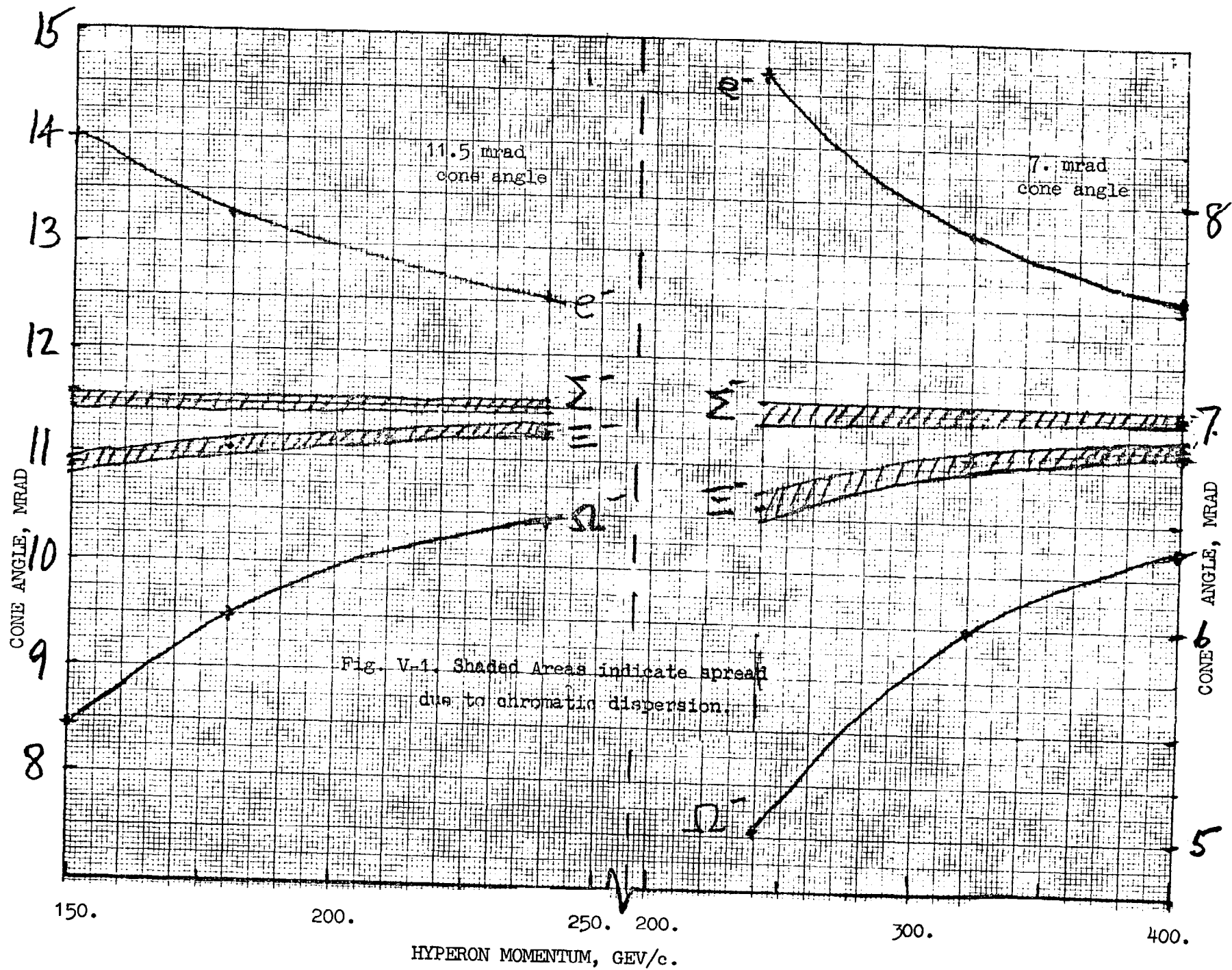


TABLE V-1

 $\Sigma^- - \Xi^-$  Separations  $\Delta\theta$ , and Chromatic DispersionCHR, in mrad. Cerenkov Cone Angle,  $\theta$ :

Hyperon Momentum GeV/c	Beam Spread, mrad*	$\theta = 7$ mrad.		$\theta = 11.5$ mrad.		$\theta = 24.5$ mrad. (DISC)	
		$\Delta\theta$ , mrad.	CHR mrad.	$\Delta\theta$ , mrad.	CHR mrad.	$\Delta\theta$ , mrad.	CHR mrad. Angular Acceptance
150	-	-	-	.603	.150	.283	(.015) .094
180	-	-	-	.420	.139	.175	(.015) .058
210	-	-	-	.307	.130		
240	.06 - .08	.387	.106	.235	.124	.111	" .037
320	.05 - .07	.217	.084	-	-	.062	" .021
360	(.06)	.172	.079	-	-	.049	" .016
400	(.06)	.140	.077	-	-	.040	" .013

\* Beam spread is due to finite target size: it is given for a 25 cm. long target.  
See Table IV-1

B. Chromatic Dispersion and How to Live with It

There are two ways to handle the chromatic dispersion problem. You can suffer its slings and arrows; or, you can take arms against it, and by opposing, end it. (The third alternative, to vacillate, Hamlet-like, we reject.).

Cerenkov detectors in which the chromatic dispersion is corrected are known by the generic name of DISC. They are usually characterized by extremely high resolution and correspondingly small angular acceptance; the last entry in Table V-1 shows a typical instrument of this type. These features of the DISC are not inherent characteristics; they are consequences of a decision to use large cone angles, which keeps the counter shorter and smaller in diameter, and thus less expensive. The latter point is of great importance, since the achromatization of the DISC, extending as it must into the UV, is very expensive.

The alternative to the DISC is to use a conventional Cerenkov focusing counter, with a considerably smaller cone angle, which improves the mass resolution. One must then accept the greater length, additional hyperon decay, and decreased light output this choice entails. If the beam optics are not able to supply a hyperon beam within the phase space acceptance of the DISC counter, one must either accept the corresponding loss of beam or switch to the conventional detector.

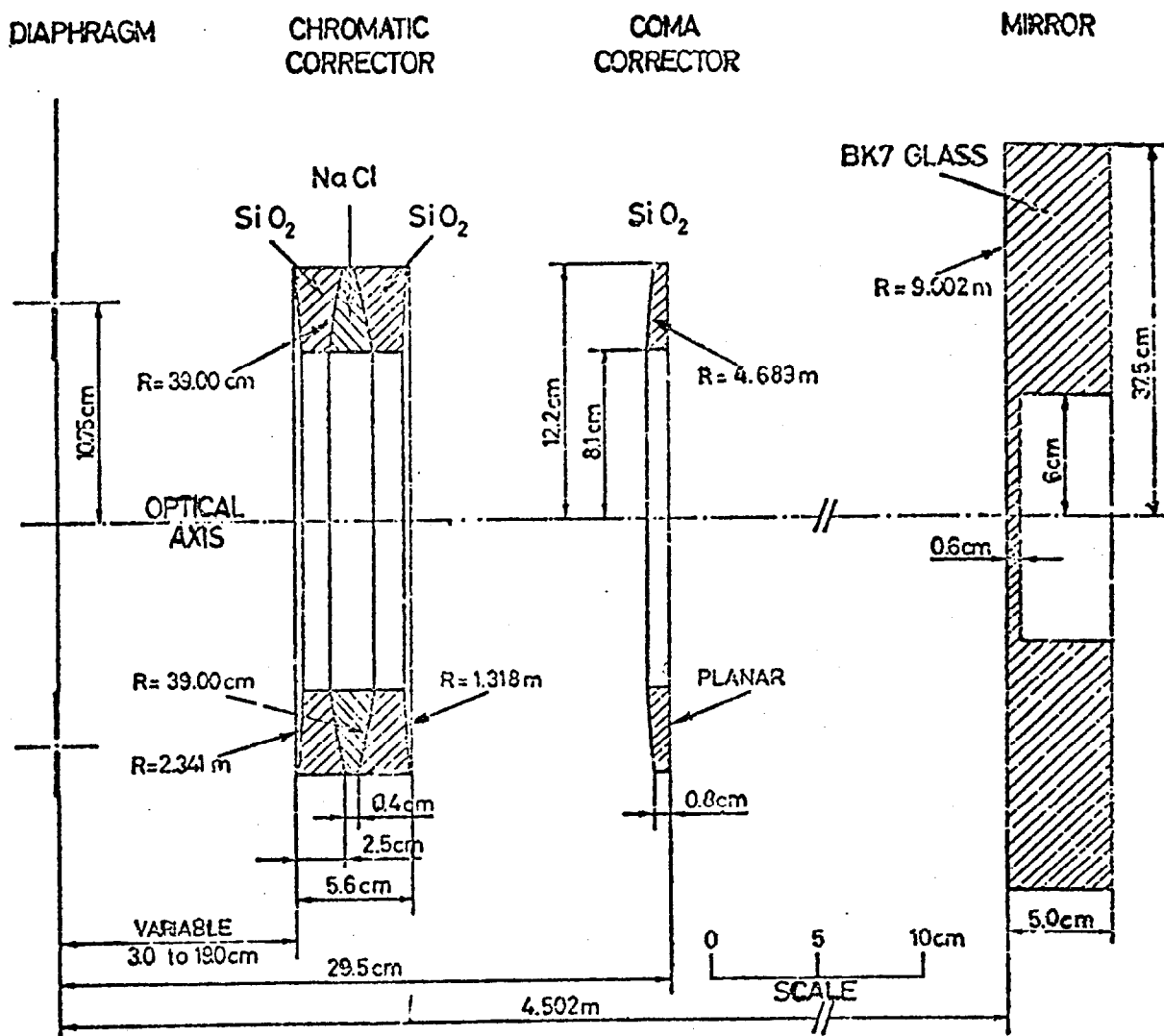
In considering whether to use a DISC or a conventional counter, we have been influenced by the fact that there exists in the Laboratory a half-completed DISC which might perhaps be

made available to this beam; it is the one whose characteristics are described in Table V-1. Figure V-2 shows a sketch of it. Considerations of both cost and procurement time probably rule out of consideration any other DISC design, and thus we confine ourselves to this one example.

C. Performance Requirements and how to Achieve Them

An ideal Cerenkov detector would detect, identify, and tag all particles traversing it, and also measure their direction and momentum. Let us see how closely such an ideal may be approached.

First, we note that the DISC does not attempt this task. It has a single circular slit, albeit of very high resolution, and detects only those particles whose Cerenkov light passes through the slit. There are no anticoincidence circuits; it rejects unwanted particles by brute force. To achieve a reasonable degree of signal purity, at least sixfold, preferably eightfold coincidences are required for the accepted particles; thus the minimum number of photons in the ring image must be in the range 30 to 40. The resolution is excellent, and the specifications on allowable angular divergence of the beam correspondingly stringent. From Table V-1 we note that at 240 GeV/c the 24.5 mrad DISC we are considering will have an angular acceptance of .037 mrad, with correspondingly less at higher momenta. In contrast, the angular divergence of the beam is determined in practice by target size; and for the 25 cm. long target we would like to use, the beam spread is as large as .06 to .08 mrad.



SPECIFICATIONS OF THE OPTICS FOR THE CERN DISC  
CERENKOV COUNTER (JULY 1971)

Fig. V-2. Internal construction of the 24.5 mrad CERN DISC counter.

Corresponding losses in detection efficiency will be inescapable.

The alternative, the conventional ring-focusing counter, does not rely on high resolution alone to distinguish particles. It accepts the chromatic aberration in the gas radiator, and circumvents it by taking advantage of the fact that the chromatic aberration is a decreasing fraction of the angular separation of any two particles of different masses, as the cone angle is decreased.

Let us assume that the Cerenkov detector can be so constructed that its cone angle and length are variable, to allow the resolution and length to be adjusted to fit the momentum in use. To obtain sufficient light, we take a radiator length of 14 meters for a cone angle of 7 mrad. We then reduce to 6 m for an 11.5 mrad cone angle; in the latter case the total light is slightly more. We add arbitrarily, 1 meter to each length to obtain overall lengths of 15 and 7 meters.

The greater length incidental to smaller cone angles increases the decay likelihood; but up to 400 GeV/c, the overall counter length increases more slowly than the relativistic dilation of the decay length, so we can afford it. The angular separation of the particles increases as the cone angle is decreased, allowing greater beam divergence, target size, and easing alignment and constructional tolerances. Furthermore, more sophisticated means of separating particles of different masses than a single fixed slit can be used, since the optics are now simpler. The method generally used to deal with more than one ring image is usually some form of image dissection.



### Image Dissection

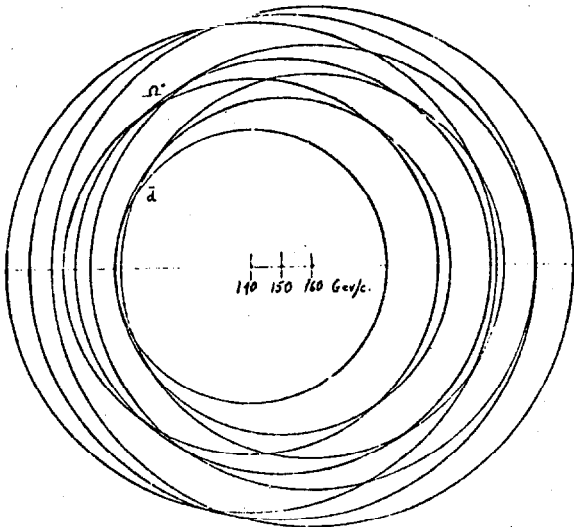
Image dissection is the most general method available for the extraction of information from complex optical images. The prototype is the television raster scan, in which the image is dissected into a series of adjacent lines, scanned in turn to make a complete frame. For this purpose storage tubes like the vidicon are preferable, since they integrate and store an image which is then read out by a scanning electron beam. This technique is available for Cerenkov images, although not in quite so simple a form; the signal-to-noise ratio of the vidicon is inadequate for signals from single photons. The deficiency can be remedied by preceding the vidicon with one or two stages of image-intensifier. This technique for storing and dissecting ring images using image intensifiers and storage phosphors was first suggested by one of us in 1960<sup>14</sup>, when the available image intensifiers were not really satisfactory. Present-day "second generation" intensifiers are, and one technique proposed for this experiment involves the use of such an image-dissecting system, using one or more channel electron multiplier array (CEMA) tube, with a segmented anode for image dissection<sup>15</sup>. In the achromatic beam the segmented anode is greatly simplified, since it becomes merely a raster in polar coordinates.

The advantage of the image dissection technique can best be understood if one imagines a Cerenkov detector whose output is a large screen on which flash the successive ring images of different particles. For each particle one can determine the

location of the center of the ring and the radius. This is all the information available; it gives the particle direction and velocity. If the particle momentum is known this determines the mass. It is the mechanization of this process that offers difficulties.

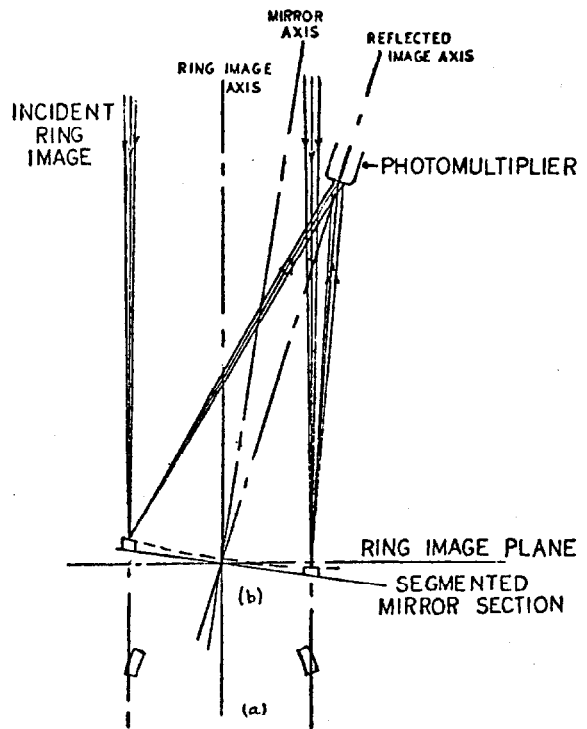
Returning to the conventional focusing Cerenkov detector, we ask: how can these results be obtained using only photomultiplier detectors, until suitable image-intensifier tubes become available? The answer clearly lies in the provision of an array of slits and photomultiplier tubes, preferably not too complicated nor too expensive.

If we now compare the requirements for the dispersive beam and the achromatic beam, the advantage of the latter becomes apparent. A method for image-dissection to identify all the hyperons in a dispersive beam was described by one of us in 1972<sup>5</sup>. It used a system of multiple slits, but replaced slit segments by mirror segments to add another element of freedom in the placement of the photomultiplier tubes. Figure V-3 shows the ring images for three different particles in a dispersive beam, at three different momenta. The considerable overlap would be much reduced by narrowing the momentum range; but on the other hand, increasing the momentum to 400 GeV/c would again make the separation more difficult as the velocity differences decrease. Furthermore, a completely new slit segmentation layout would be required for each momentum, since the relative radii change with momentum. Figure V-4 shows how the image dissection is accomplished. A similar



The Cherenkov circles for  $\Xi^-$ ,  $\Omega^-$ , and  $\bar{d}$  at 140, 150 and 160 GeV/c, showing the approximate focusing for each kind of particle, the considerable overlapping at the right hand side, and the possibility of mass determination even without using the focus. Centers for each momentum are shown.  $n=1.00011$ .

Fig V-3. Ring images in the dispersive hyperon beam.



The use of concave mirror segments in the Cherenkov ring image plane to separate and collect the light falling on a specified symmetrical pair of segments. (a) A pair of circular segments in the image plane, seen from the direction of the incident light. (b) A slight tilt of the axis of the segmented mirror results in the collection of the light in a phototube out of the way of the incident light. Note that the focus of the incident Cherenkov light must be at the mirror plane in order to use the mirror segments as velocity slits.

Fig. V-4. Image dissection with segmented mirrors.

design for CEMA tube with segmented anode structure has been proposed by J. Sandweiss<sup>15</sup>.

In contrast to Fig. V-3, now consider the achromatic beam ring images, which are merely a set of concentric circles, all the centers now being coincident. In principle, the slits can now be simple circular mirror segments. The design simplification is very great, and the performance improvement should be dramatic. Exactly similar arguments apply to the segmented-anode CEMA tube, which is the analogue of the mirror system just discussed. In this case, the rearrangement of segments required by a momentum change might be logical rather than hardware, if the anode segmentation is sufficiently fine-grained. In both cases, the image dissection is reduced by achromatization to the trivial case of a raster in polar coordinates. Figure IV-5 shows the components of a CEMA detector.

There is one point of conflict between the CEMA type image intensifier detector and the slit or mirror-imaging dissecting system using phototubes; this is the size of image required. CEMA tubes are presently limited, by cost considerations, to a maximum diameter of 40 mm. One can use several tubes, but clearly image diameters should not be much over 80 or 90 mm. On the other hand, the optics and mechanics for slit and mirror segment systems are easier for larger sizes. We consider below some possible solutions and compromises of this problem.

The image-dissection system can of course be simplified and varied. The simplest form is a slit for the accepted particle,

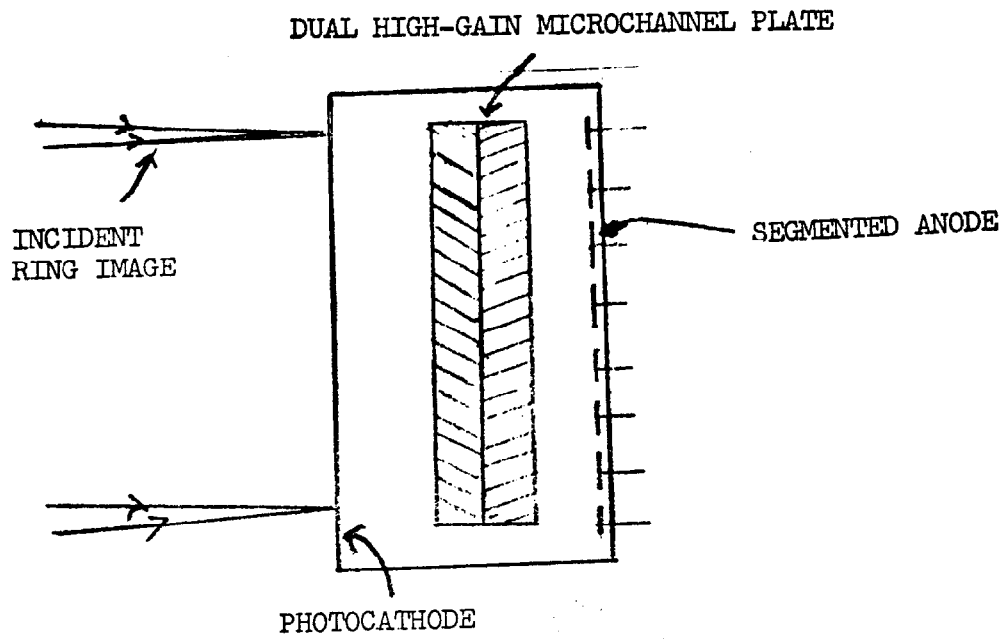


Fig. V-5a. CEMA image intensifier tube with segmented anode. Proximity focusing is used both at the cathode and anode.

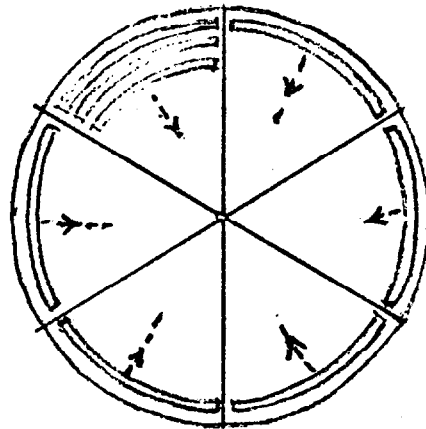


Fig. V-5b. Segmented anode, with concentric  $60^\circ$  segments. Only a few segments have been drawn in.

and mirrors for the rejected ones, in anticoincidence; this form has been used by Ozaki et al.<sup>16</sup> Versions that accept and individually tag all the hyperons can readily be envisaged. Experience with a model of a segmented mirror detector indicates that the only problem is the mechanical mounting of the mirror segments and that it is soluble, most readily when the segments are not too small.

TABLE V-2

Slit Parameters for Photomultiplier Detector System,  
with a 5.0 m Focal Length Mirror.  $\Delta\theta$  is  
the  $\Sigma^- - \Xi^-$  Angular Separation

A. 7.0 mrad cone angle (for sigmas): image radius 35 mm.					
P GeV/c	$\Delta\theta$ mrad.	Sigma-Xi sep, mm	Slit Width, mm	Cone angle, mrad for $\beta$ = 1	Max. image radius, mm
240	.387	1.935	0.75	8.6	43.0
320	.217	1.085	.62	7.82	39.1
400	.140	0.70	0.55	7.61	38.05
B. 11.5 mrad cone angle: image radius 57.5 mm.					
150	.603	3.0	1.00	14.0	70.0
180	.420	2.10	.85	13.3	66.5
210	.307	1.54	.80	12.8	64.0
240	.235	1.18	.75	12.5	62.5

#### D. Mirror Optics

The mirror optics required for the Cerenkov detectors depends not only on the length and cone angle of the Cerenkov radiator, but also on the image size required by the detector. Three different detector arrangements can readily be envisaged: one in which only conventional photomultipliers are used, one using a single 40 mm CEMA image intensifier tube, and one using several such tubes in order to obtain larger images and better resolution.

The optical quality of the mirrors is not as high as that needed for astronomy or photographic purposes, where the diffraction limit is in the region of 0.002 mrad. A mirror whose resolution is ten times worse than that would still be perfectly acceptable. Aberrations up to .02 mrad can likewise be tolerated. The size of mirror needed is given by the longest radiator, 14 m, and the largest cone angle which is 8.6 mrad. This gives a mirror aperture requirement of 120 mm radius; a 10" diameter mirror is indicated. The 11.5 mrad detector, with a much shorter (6m) radiator does not need the full diameter.

For photomultiplier detectors, with several photomultipliers - say 4 - desired per particle in order to obtain high-order coincidences for background reduction, a large image format is desirable; this makes the slits easier to make, and allows them to be closer together. Thus, a 5 meter focal length would give a maximum image diameter, with the 8.6 mrad cone mentioned above, of 86 mm. The image would be larger with the 11.5 mrad system, where a maximum cone angle of 14. mrad yields an image diameter of 140 mm.

Table V-2 shows the separations and slit widths needed for this system, for the photomultiplier detector array and a 5.0 m focal length mirror. For the arrangement using four 40 mm CEMA tubes, each one occupying a quadrant of the image (whether together or separated by dissecting the primary mirror, as suggested by Sandweiss<sup>15</sup>), the range of image radii that can be accommodated is from about 13 to 43 mm. From Table V-2, this would be entirely satisfactory with a 5 m focal length mirror for the 7 mrad cone angle, but not for the 11.5 mrad. For that angle, to keep the maximum radius within range, the focal length should not exceed 3.0 m. That mirror, however, needs a diameter of only 158 mm.

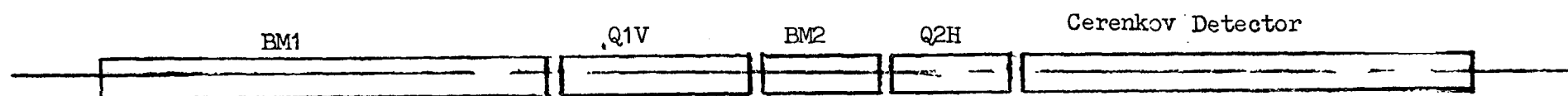
The case of the single 40 mm CEMA tube is a rather special one; it requires the best resolution in the detector because of its small area, and thus the shortest focal length mirrors. Sandweiss has estimated a focal length of about 1.25 m for this detector, which would give a maximum 35 mm diameter image at 14 mrad. It is interesting to contemplate the possibility of using a Schwarzschild optical system, as suggested by Sandweiss, with a 3 m focal length first mirror, and a second mirror to give a final focal length near 1.25 mm. To use the system with the 4-tube CEMA array, the second mirror could be replaced by a plane reflector, giving a 3 m focal length. The mirrors would have to be so figured as to be usable either singly or together.



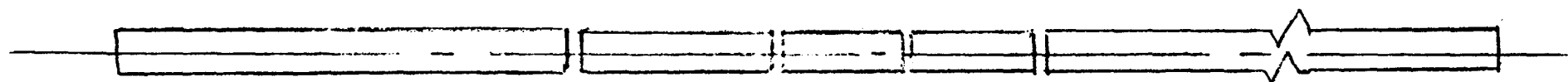
To summarize, the general design of the focusing Cerenkov detector that emerges from our considerations requires variation of the  $\Sigma^-$  cone angle from 7 to 11.5 mrad, to cover the momentum range 150 - 400 GeV/c. The length will change correspondingly from 7 to 15 meters. Distinguishing sigmas from xis should be possible for all momenta up to somewhere between 320 and 400 GeV/c. Simultaneous tagging of omega (and/or  $\bar{p}$ ) with either sigma or xi appears feasible.

Such a detector appears preferable to the DISC on the grounds of flexibility, ability to utilize the proton beam efficiently (with minimum muon background) at all energies, multiple tagging and anticoincidence possibilities, and cost.

Figure V-6 shows how the beam and Cerenkov detector system envisaged would appear.



a) 150 - 240 GeV/c. Overall length 21.5 m. Cerenkov cone angle 11.5 mrad.



b) 240 - 400 GeV/c. Overall length 29.5 m. Cerenkov Cone angle 7. mrad.

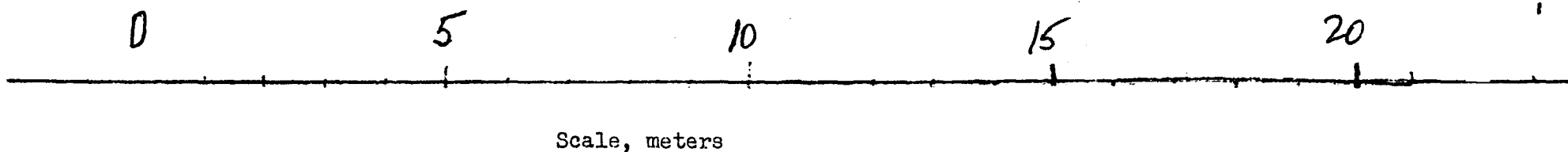


Fig. V-6. Beam layout for two different energy regions, using variable-length Cerenkov detector.

## VI. SUMMARY

1. An achromatic hyperon beam has been designed for the proton central area, to cover the momentum range 150- 400 GeV/c, with incident protons up to 500 GeV/c. It requires four superconducting magnets of special design: two dipoles and two quadrupoles. Cerenkov detectors capable of accepting all particles in the transmitted momentum interval (up to several percent) are described.

The performance of the transport and Cerenkov detector allow separation and identification of all hyperons at all energies in this range (with the possible exception of sigma-xi separation near the top end of the range.) The required proton beam will not exceed  $10^{12}$  protons per pulse, and may well be less. The incident proton beam must have as high a quality (small acceptance) as possible; it is the limiting factor in the obtainable angular and momentum resolution.

2. Calculations on muon background indicate it to be adequately low, except possibly at the lowest secondary beam momenta. If it does become a problem, steps to ameliorate it are feasible.

3. Considerations on the types of Cerenkov detector possible for use with an achromatic beam lead us to recommend a conventional focusing detector, so designed as to allow:

- a) A change of cone angle and length between the 7 mrad, 15 meters; and 11.5 mrad, 7. meters.
- b) An interchangeable optical system permitting the use of either a conventional system with photomultiplier sensors, or a CEMA detector with a segmented anode system.

We have not yet concerned ourselves with some important problems that still require attention. These include steering and focusing for the incident proton beam, and the details of the collimator in BM1.

We conclude that the achromatic beam concept is a valid and important advance; that it makes possible simple, efficient and powerful Cerenkov detectors, and the extension of the useful energy range to above 300 GeV/c; and that the beam may be designed to render the muon background innocuous. Table VI-1 summarizes the properties of dispersive and achromatic beams and the corresponding Cerenkov detectors.

TABLE VI-1

Comparison of Dispersive and Achromatic Beam  
Properties and Their Implications for Detectors

Characteristic	Dispersive	Achromatic
Momentum Range $\delta p/p$	Up to $\pm 6 - 10\%$	Up to $\pm 3\%$
Horizontal Angular Dispersion (150 GeV/c)	0.22 mr/1% $\delta p/p$	.02 mr. for $\pm 3\%$ $\delta p/p$
Vertical Angular Dispersion (150 GeV/c)	$\pm .06$ mr ( $\pm 6.6\%$ $\delta p/p$ )	$\pm .03$ mr. for $\pm 3\%$ $\delta p/p$
Method of Momentum Determination	Measurement of horizontal direction at exit.	Horizontal location at two points along beam.
Accuracy of Momentum Determination	Limited (in both cases) by target size. For small targets ( $< .2$ mm) achromatic beam may be limited by location accuracy ( $70 \mu$ ) at about $\pm 0.3\%$ .	
Sigma-Xi separation:	Fraction of beam accepted by a Cerenkov detector with .06 mr vertical aperture, at 240 GeV/c:	
	Momentum acceptance 0.3%	Momentum acc. $\pm 3\%$
	Vertical acceptance 50%	Vertical acc. 100%
Type of detector needed for detection efficiency above 10%	Special image-dissecting type; image-dissecting scheme changes with particle momentum. Conventional. (100% efficient)	
Beam length at 240 GeV/c, not including Cerenkov detector.	10.7 m	12.6 m.
Maximum momentum at which sigma-xi separation is feasible	200-240 GeV/c?	320-400 GeV/c

REFERENCES

- <sup>1</sup>Proposal, E97.
- <sup>2</sup>Proposal, P-353.
- <sup>3</sup>Fermilab Internal Report E97-1, by A. Roberts.
- <sup>4</sup>Fermilab Internal Report, A. Roberts, M. Atac, and R. Stefanski, May 7, 1970; R. Stefanski, FN-239, December 10, 1971.
- <sup>5</sup>A. Roberts, Nucl. Instr. and Meth. 99, 589 (1972).
- <sup>6</sup>V. Hungerbuehler et al., NAL Pub. 73/16 Exp; Phys. Rev. Lett. 30, 1234 (1973).
- <sup>7</sup>R. March and R. McCracken, TM-330, Nov. 1971.
- <sup>8</sup>R. Adair, private communication.
- <sup>9</sup>C. M. Ankenbrandt, Internal memo, February 27, 1975.
- <sup>10</sup>P. Sanger, private communication.
- <sup>11</sup>C. T. Murphy, private communication.
- <sup>12</sup>CERN/74-32, SPSC/P2 Add. 1, Addendum to Charged Hyperon Proposal, R. Baldi et al., March 1974.
- <sup>13</sup>C. L. Wang, Phys. Rev. D7, 2609 (1973); *ibid* D10, 3876 (1974).
- <sup>14</sup>A. Roberts, Nucl. Instr. and Meth. 9, 55 (1960).
- <sup>15</sup>Fermilab, E-97, YJS-1, June 1975: Cerenkov Counters for E-97, P-353, J. Sandweiss.
- <sup>16</sup>S. Ozaki, J. J. Russell, E. J. Sacharidis and J. T. Reed, Nucl. Inst. Meth. 35, 301 (1965).